

DRAGON: Determining Regulatory Associations using Graphical models on multi-Omic Networks

Katherine H. Shutta^{1,2,‡}, Deborah Weighill^{1,†}, Rebekka Burkholz⁶, Marouen Ben Guebila¹, Dawn L. DeMeo², Helena U. Zacharias^{3,4}, John Quackenbush^{1,2,*}, and Michael Altenbuchinger^{1,5,*}

¹Department of Biostatistics, Harvard T.H. Chan School of Public Health, Boston, MA, USA

²Channing Division of Network Medicine, Department of Medicine, Brigham and Women's Hospital and Harvard Medical School, Boston, MA, USA

³Department of Internal Medicine I, University Medical Center Schleswig-Holstein, Campus Kiel, Kiel, Germany

⁴Institute of Clinical Molecular Biology, Kiel University and University Medical Center Schleswig-Holstein, Campus Kiel, Kiel, Germany

⁵Department of Medical Bioinformatics, University Medical Center Göttingen, Göttingen, Germany

⁶CISPA Helmholtz Center for Information Security, Saarbrücken, Germany

[†]Current address: Lineberger Comprehensive Cancer Center, University of North Carolina at Chapel Hill, Chapel Hill, NC, USA

[‡]authors contributed equally to this work

*shared senior authors

Abstract

The increasing quantity of multi-omics data, such as methylomic and transcriptomic profiles, collected on the same specimen, or even on the same cell, provide a unique opportunity to explore the complex interactions that define cell phenotype and govern cellular responses to perturbations. We propose a network approach based on Gaussian Graphical Models (GGMs) that facilitates the joint analysis of paired omics data. This method, called DRAGON (Determining Regulatory Associations using Graphical models on multi-Omic Networks), calibrates its parameters to achieve an optimal trade-off between the network's complexity and estimation accuracy, while explicitly accounting for the characteristics of each of the assessed omics "layers." In simulation studies, we show that DRAGON adapts to edge density and feature size differences between omics layers, improving model inference and edge recovery compared to state-of-the-art methods. We further demonstrate in an analysis of joint transcriptome - methylome data from TCGA breast cancer specimens that DRAGON can identify key molecular mechanisms such as gene regulation via promoter methylation. In particular, we identify Transcription Factor AP-2 Beta (TFAP2B) as a potential multi-omic biomarker for basal-type breast cancer. DRAGON is available as open-source code in Python through the Network Zoo package (netZooPy v0.8; netzoo.github.io).

1 Introduction

Many biological systems can be visualized using networks, where biologically relevant elements are represented as nodes and relationships between those elements are represented as edges. Examples include gene regulatory networks, which represent the regulation of genes by transcription factors, and protein-protein interaction networks, which capture physical interactions between proteins [1, 2].

Network models can be based on prior knowledge [3], inferred from data [4], or combinations thereof [5]. Here, we focus on data-driven network inference from high-throughput multi-omic data. In this context, co-expression networks [6], which are based on a measure of correlation such as Pearson’s correlation, are often used to capture potential associations between biomolecules that may be coordinately altered in specific biological states. However, a major drawback of such networks is that they do not distinguish direct from indirect effects [7]. For example, consider a situation where a transcription factor A regulates the expression of two genes, B and C . In this case, a correlation network will contain an edge between gene B and gene C because correlation indicates a relation between the two genes. However, that relationship is only a consequence of their mutual relationship with the transcription factor A and thus the observed edge in the correlation network represents an indirect association. The problem of such erroneous correlations was discussed by Pearson and Yule in the early 20th century, where the term “spurious correlation” was introduced to distinguish indirect from direct relationships. A historical review of this question has been summarized by Aldrich and colleagues [8].

Several approaches have attempted to address this issue [9, 10, 11, 12], of which Gaussian graphical models (GGMs; also known as partial correlation networks) [11, 12] are among the most widely used methods. In a GGM, edges represent partial correlations. Intuitively, the partial correlation between two variables can be considered as the correlation that takes into account the effect of all remaining variables in the data set. Thus, it can distinguish a direct relationship from one that is mediated by one or more other variables. GGMs outperform simple correlation networks [13] and were consistently among the best in comparison to other methods in finding meaningful associations [14].

A single type of omics data generally only provides part of the information necessary to distinguish between direct and incidental relationships. For example, we know that gene regulation is a process that involves multiple layers of control, including transcription factor binding, epigenetic regulation, and chromatin structure. However, many analyses incorporate only gene expression data and not other regulatory data. Incorporating data from multiple omics could help prevent possibly erroneous conclusions based on the concept of spurious correlations introduced above.

New technologies are making it possible to generate multiple layers of omics data from the same samples. For example, The Cancer Genome Atlas (TCGA) provides data on RNA expression, methylation levels, and copy number variations for many individual tumor samples. More recently, single cell multi-omic data have become available as it has become possible to assay different omics data types from individual cells; for example, Cao et al. (2018) measured RNA and chromatin accessibility in single cells [15]. Such multifactorial data will allow us to better disentangle interactions between biological variables and distinguish genuine from spurious associations.

Most omics data are high dimensional, meaning that the number of measured variables p typically exceeds the number of samples n (or both are of the same order of magnitude), which presents challenges for network inference [7]. Several remedies have been proposed based on regularization techniques from high-dimensional statistics [11, 12, 16, 17]. Multi-omics network inference is complicated by a number of factors including the larger numbers of variables, different numbers of variables for each omics layer, variable noise levels within and between layers, and different edge densities in each data type.

In this work, we propose **DRAGON** (**D**etermining **R**egulatory **A**ssociations using **G**raphical models on multi-**O**mic **N**etworks), a machine learning method to estimate GGMs using two omics layers simultaneously. DRAGON calibrates omic-specific parameters for each omic layer to achieve an optimal trade-off between model complexity and estimation accuracy while explicitly taking into account the unique characteristics of each omics layer.

We show in simulations that DRAGON adapts to differences in edge densities and feature sizes of the included omics layers. Finally, we use DRAGON to analyze joint transcriptome–methylome data from TCGA breast cancer specimens. The latter analysis shows that DRAGON can identify potential regulatory molecular mechanisms, such as the association between promoter methylation and gene expression. We further show that DRAGON can identify multi-omic biomarkers, as exemplified by the combination of promoter methylation and gene-expression of TFAP2B (Transcription Factor AP-2 Beta), which is strongly associated with the basal-like breast cancer subtype.

2 Materials and Methods

2.1 The Gaussian Graphical Model

Let X be a $n \times p$ data matrix of n observations (samples) and p features (such as genes, methylated sites, or proteins). Assume that the observations $\mathbf{x}_1, \mathbf{x}_2, \dots, \mathbf{x}_n \in \mathbb{R}^p$ are independent and identically distributed according to a multivariate normal, $N(\mu, \Sigma)$, where Σ is a positive definite covariance matrix. Further, $\Theta = (\theta_{ij}) = \Sigma^{-1}$ is the inverse covariance matrix (also called precision matrix) where vanishing entries θ_{ij} correspond to conditional independencies between variables i and j . A Gaussian Graphical Model (GGM) is a conditional dependence graph in which nodes represent variables and edges connect conditionally dependent pairs of variables [18, 19].

Let $S = \frac{1}{n} \sum_{i=1}^n (\mathbf{x}_i - \hat{\mu})(\mathbf{x}_i - \hat{\mu})^T$ be the sample covariance matrix, where $\hat{\mu} = \frac{1}{n} \sum_{i=1}^n \mathbf{x}_i$ is the sample mean. Then, the corresponding log likelihood takes the form

$$l(\Theta) = \frac{n}{2} (\log |\Theta| - \text{Tr}(S\Theta)). \quad (1)$$

2.2 Covariance shrinkage

The Maximum Likelihood Estimate (MLE) of Eq. (1) yields $\hat{\Theta} = S^{-1}$. However, if the number of features p exceeds the number of independent observations n , then S is singular and cannot be inverted. Even if p is smaller than n but of the same order of magnitude, $\hat{\Theta}$ has a high variance. One way this issue is often addressed by adding regularization terms to Eq. (1), as for example proposed in [17]. Another approach is that of Schäfer and colleagues [12], who bias the covariance matrix towards a target matrix that is typically full-rank. Such “covariance shrinkage” is based on the biased estimator

$$\hat{\Theta} = ((1 - \lambda)S + \lambda T)^{-1}, \quad (2)$$

where $\lambda \in [0, 1]$ is a regularization parameter that can be estimated using the Lemma of Ledoit & Wolf [20] and T is the target matrix. Here, different choices for T have been proposed, such as the identity, $T = I_p$, and the diagonal of S , $T = \text{diag}(s_{11}, s_{22}, \dots, s_{pp})$. The idea behind Eq. (2) is to replace the empirical covariance S in the MLE of Θ by a linear combination of S and the target matrix T representing conditional independence. Because T is full-rank, the singularity of S is mitigated in this sum. Consequently, a biased precision matrix estimator can be obtained from inverting the shrunken covariance matrix. Throughout this article, we use the target matrix $T = \text{diag}(s_{11}, s_{22}, \dots, s_{pp})$ following the arguments in [12].

2.3 DRAGON

2.3.1 Generalized covariance shrinkage

In DRAGON, we extend covariance shrinkage to account for two different omics layers by introducing layer-specific regularization terms. Let $X^{(1)}$ be a $n \times p_1$ data matrix that represents the first omics layer and let $X^{(2)}$ be a $n \times p_2$ data matrix for the second layer, where p_1 and p_2 are the number of variables from omics layers 1 and 2. We further assume paired data, meaning that measurements (rows) $\mathbf{x}_i^{(1)}$ and $\mathbf{x}_i^{(2)}$ correspond to the same sample i but differ in their features. We define the empirical covariances $S^{(k,l)} = \frac{1}{n} \sum_{i=1}^n (\mathbf{x}_i^{(k)} - \hat{\mu}^{(k)})(\mathbf{x}_i^{(l)} - \hat{\mu}^{(l)})^T$ with the empirical mean vector $\hat{\mu}^{(k)} = \frac{1}{n} \sum_{i=1}^n \mathbf{x}_i^{(k)}$

for $k, l \in \{1, 2\}$. Now, we can generalize the shrinkage estimator to

$$\hat{\Theta} = \left(\begin{pmatrix} (1 - \lambda_1)S^{(1,1)} & \sqrt{1 - \lambda_1}\sqrt{1 - \lambda_2}S^{(1,2)} \\ \sqrt{1 - \lambda_1}\sqrt{1 - \lambda_2}S^{(2,1)} & (1 - \lambda_2)S^{(2,2)} \end{pmatrix} + \begin{pmatrix} \lambda_1 T^{(1)} & 0 \\ 0 & \lambda_2 T^{(2)} \end{pmatrix} \right)^{-1}, \quad (3)$$

with $\lambda_k \in [0, 1]$ and $T^{(k)} = \text{diag}(s_{11}^{(k)}, s_{22}^{(k)}, \dots, s_{p_k p_k}^{(k)})$, where $S^{(k,k)} = (s_{ij}^{(k)})$. For illustration purposes, we first consider the limit $\lambda_2 = 1$. Here, Eq. (3) becomes

$$\begin{aligned} \hat{\Theta} &= \left(\begin{pmatrix} (1 - \lambda_1)S^{(1,1)} & 0 \\ 0 & 0 \end{pmatrix} + \begin{pmatrix} \lambda_1 T^{(1)} & 0 \\ 0 & T^{(2)} \end{pmatrix} \right)^{-1} \\ &= \begin{pmatrix} \Theta^{(1,1)} & 0 \\ 0 & (T^{(2)})^{-1} \end{pmatrix}, \end{aligned} \quad (4)$$

where $\Theta^{(1,1)} = ((1 - \lambda_1)S^{(1,1)} + \lambda_1 T^{(1)})^{-1}$ is the shrinkage estimator of the precision matrix using only the features with $k = 1$. Thus, if $\lambda_2 = 1$, technology 1 decouples from technology 2.

Next, consider the limit $\lambda_1 = \lambda_2 = \lambda$. Then Eq. (3) becomes

$$\begin{aligned} \hat{\Theta} &= \left((1 - \lambda) \begin{pmatrix} S^{(1,1)} & S^{(1,2)} \\ S^{(2,1)} & S^{(2,2)} \end{pmatrix} + \lambda \begin{pmatrix} T^{(1)} & 0 \\ 0 & T^{(2)} \end{pmatrix} \right)^{-1} \\ &= ((1 - \lambda)S + \lambda T)^{-1}. \end{aligned} \quad (5)$$

Thus we naively treat both omics layers as if they were generated using the same technology. These examples show that DRAGON naturally incorporates two limits that bound the optimal solution: (i) GGMs estimated for the two omics layers separately and (ii) a GGM treating both layers such as if they belong to the same layer.

2.3.2 Generalization of the Lemma of Ledoit & Wolf

The penalty parameters λ_1 and λ_2 can be estimated using cross-validation or resampling; however, such approaches are computationally expensive. Alternatively, one can use an analytical estimate following the arguments of Ledoit & Wolf [20]. There, the shrinkage parameter λ was derived by minimizing

$$R = \mathbb{E} \left[\|\hat{\Sigma} - \Sigma\|_F^2 \right] \quad (6)$$

with respect to λ , where $\hat{\Sigma} = (1 - \lambda)S + \lambda T$ and Σ is the true, underlying covariance. This is possible since $\text{bias}(S) = 0$ makes Eq. (6) independent of Σ .

Here, we extend this approach to the shrinkage formula (3) and estimate λ_1 and λ_2 by minimizing

$$\mathbb{E} \left[\|\hat{\Sigma} - \Sigma\|_F^2 \right] = \sum_{k,l=1}^2 \mathbb{E} \left[\|\hat{\Sigma}^{(k,l)} - \Sigma^{(k,l)}\|_F^2 \right] \quad (7)$$

with respect to λ_1 and λ_2 , where $\|\cdot\|_F$ is the Frobenius norm. Following the arguments in [12] (see Suppl. Section 1), we obtain

$$\begin{aligned} R &= \mathbb{E} \left[\|\hat{\Sigma} - \Sigma\|_F^2 \right] \\ &= \text{const.} + \lambda_1 T_1^{(1)} + \lambda_2 T_1^{(2)} + \lambda_1^2 T_2^{(1)} + \lambda_2^2 T_2^{(2)} \\ &\quad + \lambda_1 \lambda_2 T_3 + \sqrt{1 - \lambda_1} \sqrt{1 - \lambda_2} T_4 \end{aligned} \quad (8)$$

where the constant term is independent of λ_1 and λ_2 , and

$$\begin{aligned} T_1^{(k)} &= -2 \left(\sum_{i \neq j} \text{var}(s_{ij}^{(k)}) + \sum_{i,j} \text{E}((s_{ij}^{(1,2)})^2) \right), \\ T_2^{(k)} &= \sum_{i \neq j} \text{E}((s_{ij}^{(k)})^2), \\ T_3 &= 2 \sum_{i,j} \text{E}((s_{ij}^{(1,2)})^2), \\ T_4 &= 4 \sum_{i,j} \left(\text{var}(s_{ij}^{(1,2)}) - \text{E}((s_{ij}^{(1,2)})^2) \right) \end{aligned}$$

Eq. (8) can be easily minimized with respect to $\lambda_1 \in [0, 1]$ and $\lambda_2 \in [0, 1]$, where the moments can be estimated following [12].

2.3.3 Hypotheses testing

An estimate for the partial correlation between variable i and j can be directly obtained from $\hat{\Theta} = (\hat{\theta}_{ij})$ by calculating

$$\hat{\rho}_{ij} = -\frac{\hat{\theta}_{ij}}{\sqrt{\hat{\theta}_{ii}\hat{\theta}_{jj}}}. \quad (9)$$

As a consequence of covariance shrinkage, the partial correlation matrix $\hat{P} = (\hat{\rho}_{ij})$ is also shrunken [21]. Bernal et al. (2019) developed a null-model probability density that naturally accounts for this shrinkage effect [21]:

$$f_0^\lambda(\rho) = \frac{((1-\lambda)^2 - \rho^2)^{(\kappa-3)/2}}{\text{Beta}(\frac{1}{2}, \frac{\kappa-1}{2})(1-\lambda)^{\kappa-2}}, \quad (10)$$

where the parameter κ is given by $n - 1 - (p - 2)$ for $n \gg p$, or can be fitted by MLE for the ill-posed case $p < n$ or for $p \approx n$ [21]. For an intuitive derivation of Eq. (10) see [21]. Let

$$\hat{\Theta} = \begin{pmatrix} \hat{\Theta}^{(1,1)} & \hat{\Theta}^{(1,2)} \\ \hat{\Theta}^{(2,1)} & \hat{\Theta}^{(2,2)} \end{pmatrix} \quad \text{and} \quad \hat{P} = \begin{pmatrix} \hat{P}^{(1,1)} & \hat{P}^{(1,2)} \\ \hat{P}^{(2,1)} & \hat{P}^{(2,2)} \end{pmatrix}, \quad (11)$$

where $\hat{\Theta}^{(1,1)}$ ($\hat{P}^{(1,1)}$) has dimension $p_1 \times p_1$ and $\hat{\Theta}^{(2,2)}$ ($\hat{P}^{(2,2)}$) dimension $p_2 \times p_2$. Then, DRAGON assigns significance levels to partial correlations using the following steps:

- (i) Simulate data under the null hypotheses ($H_0 : \rho = 0$) for given sample size n , and estimate corresponding partial correlations using DRAGON with λ_1 and λ_2 given from the original data.
- (ii) Fit κ using MLE of Eq. (10) for $P^{(1,1)}$, $P^{(1,2)}$, and $P^{(2,2)}$, separately.
- (iii) Use density Eq. (10) with κ determined in (ii) to assign significance levels to $\hat{P}^{(1,1)}$, $\hat{P}^{(1,2)}$, $\hat{P}^{(2,2)}$, respectively.
- (iv) Adjust significance levels in layer (1, 1), (1, 2), and (2, 2) for multiple testing, separately, using the method of Benjamini and Hochberg [22]. Note that if we control the false discovery rate (FDR) at level α in each layer, we also control the overall FDR at level α across all layers. However, to provide good estimates, p_1 and p_2 must be assumed to be sufficiently large.

For $n \gg p$, κ is given by $\kappa = n - 1 - (p - 2)$ and (i - ii) are not necessary.

2.4 Performance comparisons

To benchmark the performance of DRAGON, we selected five methods for GGM estimation, each of which has distinct advantages and disadvantages [7], based on the requirement that they are available through a user-friendly software, provide estimates for p -values without computationally expensive resampling, and have been published in peer-reviewed journals.

- **GGM:** we implemented an omics-layer agnostic DRAGON model, which we simply denote as Gaussian Graphical Model (GGM) in the following. Note, in contrast to the GeneNet implementation described below [23], this approach uses the exact null distribution for shrunken partial correlations as suggested by [21].
- **GeneNet:** the R-package “GeneNet” [23] uses covariance shrinkage and provides estimates for adjusted p -values (q -values) via an empirical Bayes approach [24]. We used the standard settings for all comparisons.
- **B-NW-SL:** the bivariate nodewise scaled lasso was suggested by [25] and uses a regression approach to obtain asymptotically efficient estimates of the precision matrix under a sparseness condition relative to the sample size. We used the implementation provided in the “SILGGM” R-package [26] with standard settings.
- **D-S-NW-SL:** the de-sparsified nodewise scaled lasso [27] uses a modification of the nodewise lasso regression approach suggested by [16] with a de-sparsified estimator. We used the “SILGGM” R-package [26] with standard settings.
- **D-S-GL:** the de-sparsified graphical lasso was proposed by [28] and is based on a de-sparsified modification of the graphical lasso proposed by [17]. We used the “SILGGM” R-package [26] with standard settings.

For all methods except GeneNet, which provides adjusted p -values (q -values), we adjusted p -values using the procedure of Benjamini and Hochberg [22].

3 Results and Discussion

3.1 Simulation studies

We begin by briefly reviewing the concept of partial correlations and their relevance for multi-omics data analysis. Subsequently, we use four different simulation studies to show a comprehensive performance comparison between DRAGON and competing methods for GGM estimation.

Multiple layers of interacting regulatory processes are involved in determining a cell’s state. By considering molecular variables of a single omic layer, such as the transcriptome, we can miss relevant information which might lead to erroneous conclusions about causal associations. To illustrate this effect, consider a scenario where the transcription of two genes, A and B , is regulated via the same molecular (*regulator*) “variable”. The *regulator* might belong to another omics layer representing a different biological factor such as the chromatin state in the DNA region of A and B . We generated artificial data representing such a process for $n = 100$ observations (Suppl. Section 2, Fig. 1d), assuming a linear relationship between the observed level of the *regulator* and that of gene A , and between the *regulator* and gene B . Fig. 1b shows the corresponding correlation network and Fig. 1d shows the estimated Pearson correlations, r , showing a high correlation between A and B (in red, $r \sim 0.91$ and $p < 0.001$). This correlation is statistically significant although gene A and gene B are not directly related – rather, they are only co-regulated by the *regulator*. In contrast, the partial correlation between A and B takes into account the effect of the *regulator*, resulting in a non-significant partial correlation of $\rho \sim 0.02$ (Fig. 1c, using standard partial correlation) and a partial correlation network that does not have an edge between A and B (Fig. 1c), better reflecting the ground truth (Fig. 1a). Thus, if the *regulator* is included in the model, it is statistically possible to disentangle direct and indirect linear relationships.

In this section, we systematically analyze potential issues in estimating partial correlations between variables of different omics layers, and compare how different methods, including DRAGON, are affected

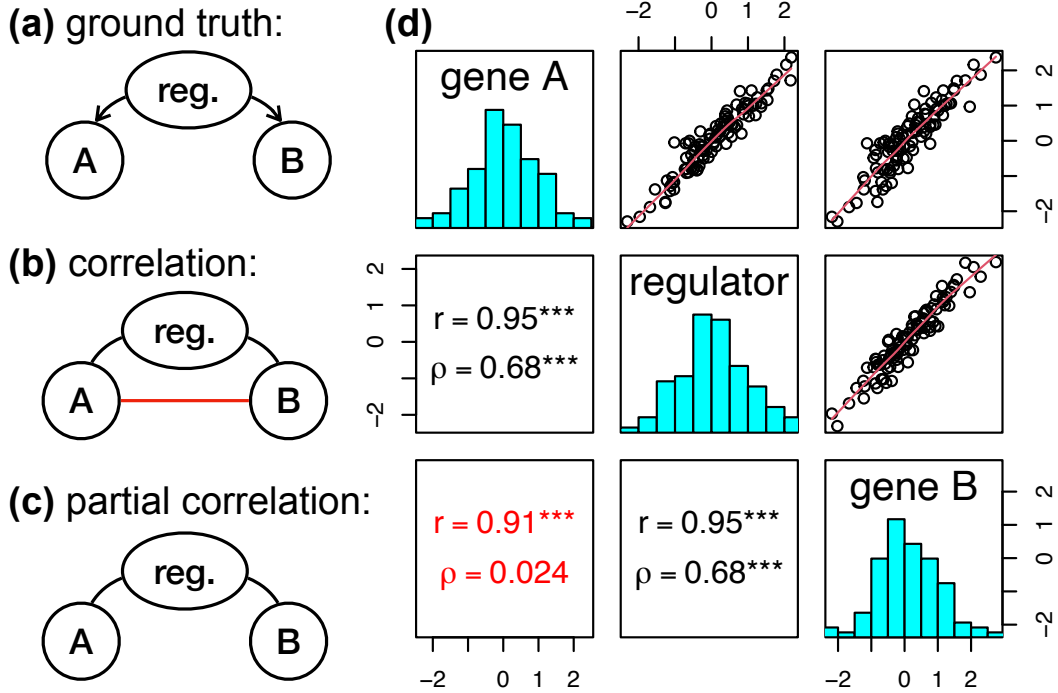


Figure 1: Partial correlation versus Pearson’s correlation on artificial data. The left figure shows from top to bottom: (a) the ground truth (directed), (b) the inferred correlation network (undirected), and (c) the inferred partial correlation network (undirected). Direct relationships are shown in black. Pearson’s correlation erroneously infers a relationship between A and B (Fig. a, red edge). Partial correlation correctly removes this relationship (Fig. c). The right figure (Fig. d) shows the corresponding data as scatterplots (upper half of the matrix) and histograms (diagonal). Corresponding Pearson’s correlation, r , and partial correlations, ρ , are given in the lower triangular matrix. Significance levels $p < 0.001$ are marked by three asterisks.

by these issues. In our simulations, we considered both high-dimensional settings (many molecular variables) as well as models in which there are different probabilities for direct relationships among variables within and between different omics layers. Table 1 describes the simulation study design in detail.

We performed four simulation studies, A to D , with fixed numbers of molecular variables, $p_1 = 100$ and $p_2 = 500$ for omics layer 1 and 2, respectively. Direct relationships can be simulated by appropriate choice of the entries of the precision matrices $\hat{\Theta}^{(k,l)}$ which parameterize the multivariate Gaussian distribution. Different simulation runs correspond to different precision matrices, which were randomly generated as follows:

- (0) start with a p -dimensional identity matrix, where $p = p_1 + p_2$,
- (1) randomly replace a proportion $\eta^{(k,l)}$ of zeros by values drawn from a uniform distribution ranging from -1 to 1 ,
- (2) replace the diagonal entries θ_{ii} by $\sum_j |\theta_{ij}|$ plus a small positive value ($\epsilon = 0.0001$) so that the precision matrix is invertible,
- (3) normalize the entries θ_{ij} of the precision matrix by $\sqrt{\theta_{ii}\theta_{jj}}$.

Each precision matrix was used to sample from a multivariate normal with mean vector $\mu = 0$ and covariance $\hat{\Theta}^{-1}$. Finally, we added a noise $\epsilon \sim N(\mu = 0, \sigma = 0.1)$ to each entry of the data matrix.

Table 1: Edge densities and edge numbers for simulation studies A , B , C , and D .

(k, l)	$(1, 1)$		$(1, 2)$		$(2, 2)$	
	η	edges	η	edges	η	edges
A	0.05	248	0.05	2500	0.05	6238
B	0.05	248	0.05	2500	0.005	624
C	0.05	248	0.005	250	0.005	624
D	0.101	500	0.01	500	0.004	500

3.1.1 DRAGON adapts to the data by dynamically chosen penalty parameters and improves model inference.

DRAGON uses an analytical estimate of the minimum of R , Eq. (6). Here, we show that this estimate dynamically adapts to sample and feature size, and to edge densities $\eta^{(k,l)}$ across a broad range of simulation settings.

Parameter recovery in Simulation A In simulation study A , the two omics layers have equal edge densities $\eta^{(1,1)} = \eta^{(1,2)} = \eta^{(2,2)} = 0.05$. Figures 2a and c show R in dependency of λ_1 and λ_2 for the analytical estimate and the ground truth, respectively, for a fixed sample size of $n = 5000$. We observed that estimate and ground truth agree remarkably well, and that they provide almost identical estimates for the position of the minimum of the selected penalty parameters, $(\hat{\lambda}_1, \hat{\lambda}_2)$. The GGM estimated according to Eq. (2) using the appended data $X = [X^{(1)}, X^{(2)}]$ corresponds to the diagonal red lines, such that the two data layers are treated as they would belong to one layer and a single regularization parameter $\lambda_1 = \lambda_2 = \lambda$ is estimated. We observed that DRAGON correctly estimated $(\hat{\lambda}_1, \hat{\lambda}_2)$ to be near to the diagonal for this simulation study. Supplementary Figures S1 and S2 confirm this finding for lower sample sizes, $n = 500$ and $n = 1000$, respectively.

Parameter recovery in Simulation B In Simulation B, we investigated the influence of the edge densities $\eta^{(k,l)}$ on R . For this, we reduced the edge density $\eta^{(2,2)}$ to $\eta^{(2,2)} = 0.005$. Again, we observed a remarkable agreement between estimated and true R , shown in Figure 2b and d, respectively, which is also the case for the estimated minima $(\hat{\lambda}_1, \hat{\lambda}_2)$. Note, $\hat{\lambda}_1$ now strongly differs from $\hat{\lambda}_2$. Since $\lambda_2 > \lambda_1$, the second omics data layer is stronger penalized than the first.

Parameter recovery in Simulations C and D We repeated this analysis for two further simulation studies, C and D , both of which have unbalanced edge densities with results shown in supplementary Figure S3, S4, and S5 for $n = 500$, $n = 1,000$, and $n = 5,000$, respectively. Here, we also found that DRAGON correctly estimates R and that λ_1 and λ_2 are chosen by the algorithm accordingly to minimize R .

Model inference in Simulations A-D We next analyzed how the DRAGON regularization scheme, which augments covariance shrinkage by omics layer-specific regularization parameters, affects model inference. We repeated simulation studies A to D 20 times for different sample sizes n and evaluated the log-likelihood on $n = 1,000$ test samples (Figure S6). While we recognize that few omics studies have 1,000 or more samples, single-cell experiments generally assay thousands of cells and large cohort studies are beginning to develop omics databases that include populations of this size or larger.

We found similar results on an absolute scale (Figures S6a to d). However, results were clearly in favor of DRAGON when we evaluated the log-likelihood difference (Figures S6e to h). This measure has the advantage that it removes variability due to different simulation runs. The green line corresponds to the median log-likelihood difference and the error bands to the 25% and 75% percentiles. Results were slightly in favor of the GGM for the balanced study A , but in situations B , C , and D , DRAGON outperformed the standard GGM as indicated by positive values for the difference. The greatest improvements were seen for the unbalanced simulation B . We can also see that as the sample size n increases with the number of predictors p remaining fixed, DRAGON and GGM estimates coincide, as demonstrated by a vanishing log-likelihood difference.

3.1.2 DRAGON outperforms the state of the art with respect to edge recovery

Adjusted p -values (q -values) were assigned as described in the Materials and Methods section and were used to assess the edge-recovery performance in simulations A to D using receiver operating characteristic (ROC) curves for DRAGON, GGM, GeneNet, B-NW-SL, D-S-NW-SL, and D-S-GL.

Table 2: Lower bounds on n and upper bounds on p/n necessary to achieve confidence in edge recovery defined via an $\text{AUC} > 0.8$ in simulation studies A , B , C , and D . Best performance is indicated in boldface letters.

simulation:	A		B		C		D	
	n	p/n	n	p/n	n	p/n	n	p/n
DRAGON	4096	0.15	256	2.34	128	4.69	181	3.31
GeneNet	4096	0.15	1024	0.59	181	3.31	512	1.17
B-NW-SL	4096	0.15	1024	0.59	181	3.31	362	1.66
D-S-NW-SL	4096	0.15	1448	0.41	512	1.17	1024	0.59
D-S-GL	4096	0.15	1448	0.41	724	0.83	1024	0.59
GGM	4096	0.15	1024	0.59	181	3.31	512	1.17

We first compared the results of DRAGON and GGM inference methods. Figure 3a shows how the area under the ROC curve (AUC) depends on the number of training samples n for simulation study A . We saw almost identical performance for DRAGON (blue) and GGM (red) for all sample sizes in our simulation, a result consistent with our previous findings. For simulation studies B , C , and D , the corresponding results are shown in Figures 3b to d and illustrate substantial improvements for DRAGON compared to GGM. For example, in simulation study B , DRAGON achieved an AUC for $n \approx 200$ samples that is compatible to that of the GGM for $n \approx 1,000$ samples. This improved performance of DRAGON is further illustrated by Figures 4a to d that shows the respective AUC differences; we found AUC improvements up to ~ 0.14 (study B), ~ 0.05 (study C) and ~ 0.13 (study D). In the balanced simulation scenario A where we expect the GGM and DRAGON to have similar performance, the GGM negligibly outperformed DRAGON, as shown by small negative values in Figure 4a. As an alternative performance assessment, we used the average area under the precision-recall curve (AUC-PR) (Suppl. Fig. S7). These results also show the performance advantages of DRAGON compared to GGM with AUC-PR differences up to ~ 0.07 , ~ 0.03 , ~ 0.08 , for studies B to D , respectively.

Analogous AUC analyses were performed comparing DRAGON with GeneNet, B-NW-SL, D-S-NW-SL, and D-S-GL with results shown in Figures 3e to t and 4e to t. Corresponding AUC-PR curves and AUC-PR differences are shown in Suppl. Figures S7 and S8, respectively. For both AUC and AUC-PR, we found in simulated data sets A , B , and D that DRAGON’s improved estimates are of the same size (for GeneNet and B-NW-SL) or substantially larger (for D-S-NW-SL and D-S-GL) than we found in comparing DRAGON to GGM. In simulation study C , we found comparable performance of GeneNet and DRAGON across a large range of sample sizes (Fig. 3g and 4g) but that GeneNet produced an inflated FDR (Suppl. Fig. S9g). Table 2 summarizes the minimum number of samples n (as well as upper bounds on p/n) for each of the simulation studies required to reach network confidence levels $\text{AUC} > 0.8$. As can be seen, DRAGON reached confidence for substantially smaller n and larger p/n ratios than the other methods.

We also verified that DRAGON correctly estimates p -values and false discovery rates (FDRs). First, we performed simulations under the null hypothesis of no partial correlation ($\rho = 0$) and verified that the p -value distributions are flat for different sets of the regularization parameters λ_1 and λ_2 (Figures S12 - 13). The simulated data sets were motivated as follows: we recorded the λ_1 and λ_2 values for each simulation run in study A to D , which yielded the results shown in Figure S12. We extracted the corresponding parameter sets at $n = 256$, $n = 1,024$ and $n = 4,096$ samples, which correspond respectively to a highly regularized estimate, a moderately regularized one, and one with low regularization. This resulted, in total, in 12 pairs (λ_1, λ_2) with the associated p -value distributions under the null hypothesis that are shown in Supplementary Figure S13; as desired, these distributions are flat. Further, we recorded the FDRs corresponding to studies A to D (Supplementary Figures S9a to d and S11) for the empirical estimate of κ and the theoretical value $\kappa = n - 1 - (p - 2)$, respectively. As expected, the observed FDR for DRAGON approaches 0.05 as the sample size increases. Analogous plots for the comparison methods can be found in Supplementary Figure S9e-t. DRAGON generally outperforms the other methods, some of which show inflated FDRs indicating an overly liberal method (GeneNet) or deflated FDRs indicating an overly conservative method (D-S-NW-SL and D-S-GL).

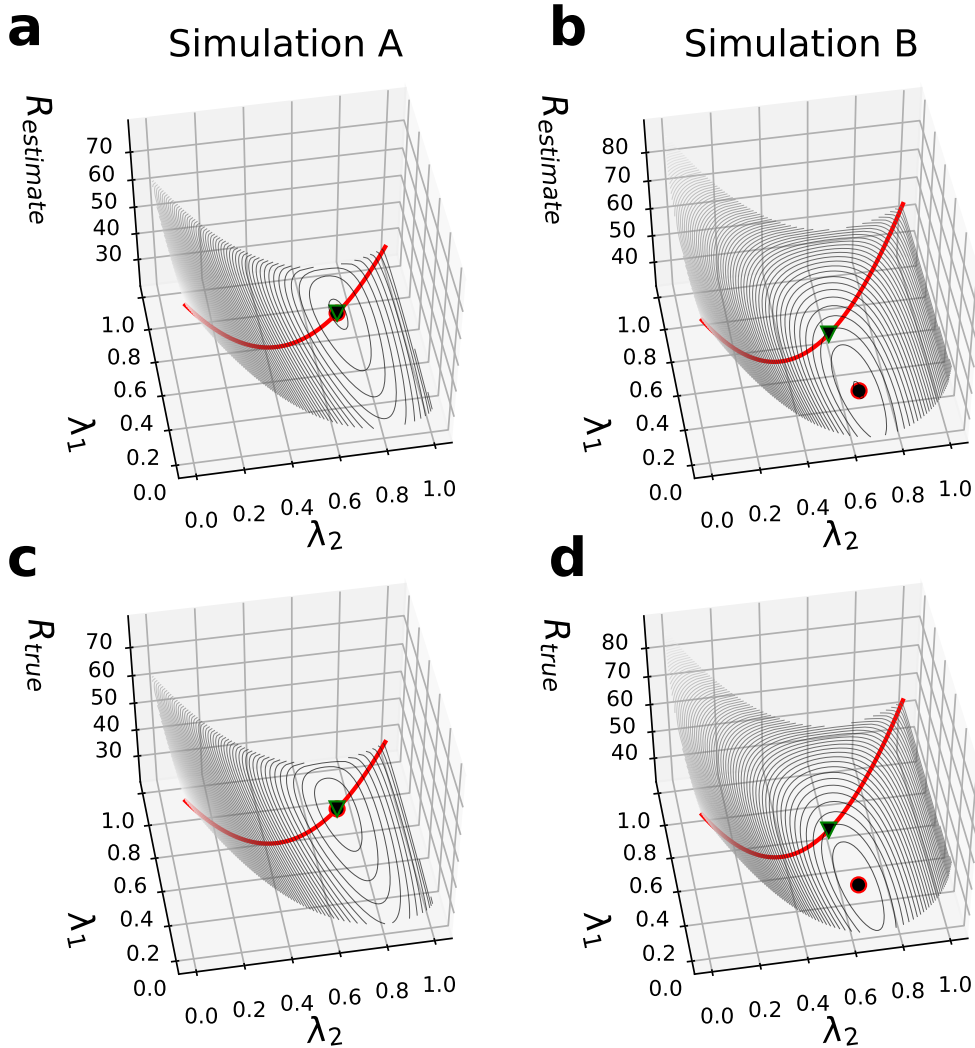


Figure 2: Parameter landscapes for DRAGON. Estimated and true R (upper and lower row) in dependency of λ_1 and λ_2 in simulation studies A (left column) and B (right column). Figures a and b show the estimated R for study A and B , respectively. Figure c and d show the corresponding ground truth. The red circles indicate the minima for each plot in the λ_1 - λ_2 plane, and the green triangles give the minima on the diagonal R values shown in red, corresponding to the standard GGM.

3.2 Integrative DRAGON analysis of transcriptome and methylome in TCGA breast cancer specimens

Epigenetic aberrations such as DNA methylation are associated with altered patterns of gene regulation during the development and progression of complex diseases such as cancer [29]. Given the performance advantages of DRAGON over other partial correlation methods, here we present an illustrative application of DRAGON to integrate promoter methylation and gene expression data in 765 breast cancer specimens from The Cancer Genome Atlas (TCGA) [30]. We began with a list of 1,590 human transcription factors (TFs) [31], of which 1,557 had annotated promoter methylation data in TCGA, 1,311 had gene expression data, and 1,297 TFs had both. Below, we outline the analysis of these data; further details regarding the sample population, data preprocessing, model inference, community detection and Reactome pathway enrichment analysis are summarized in Supplementary Sections 4 and 5.

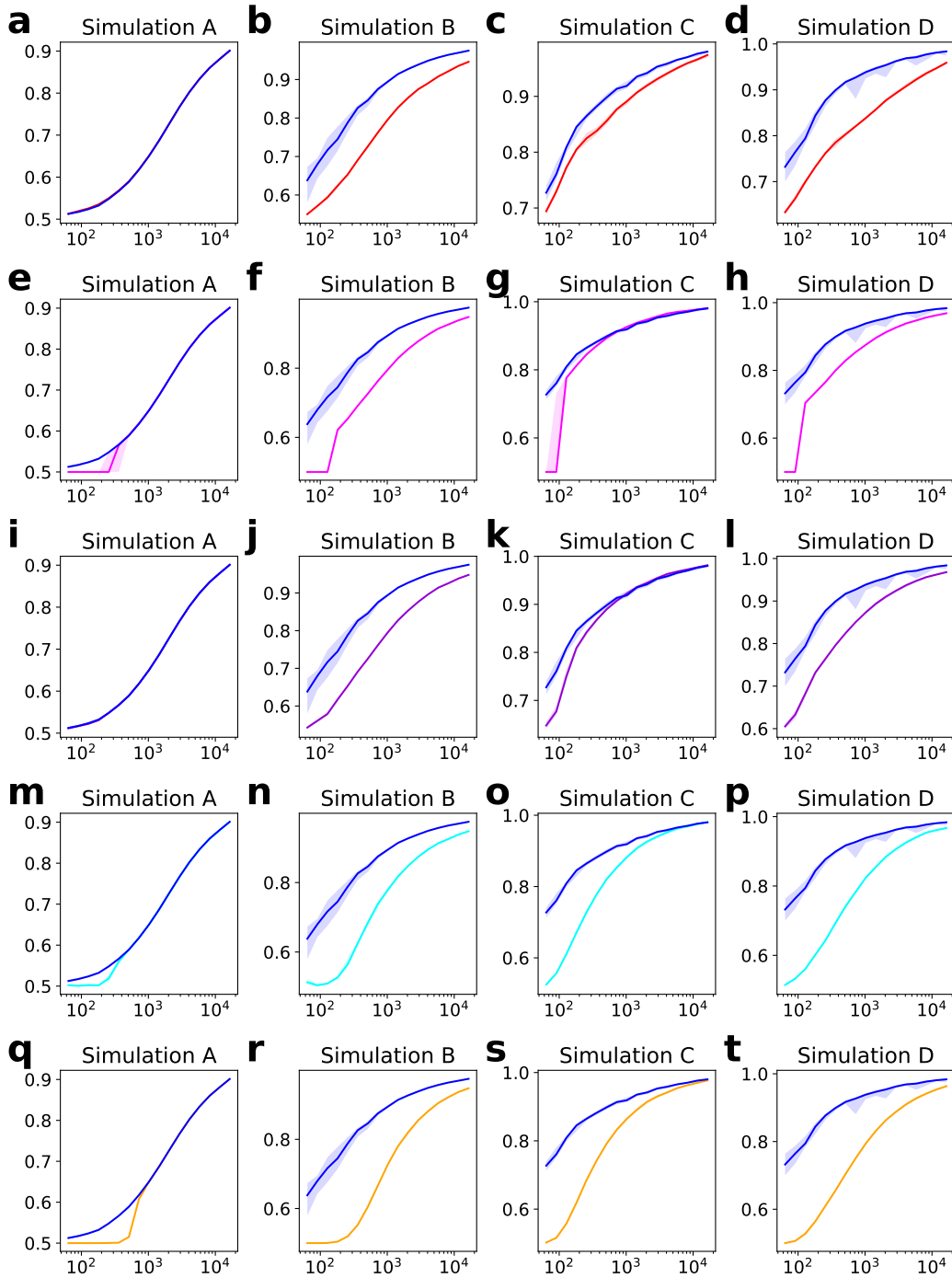


Figure 3: Area under the ROC curve (AUC) for edge-recovery performance versus sample size n of simulation studies A to D (columns). Each row compares DRAGON (blue) with GGM (red, Fig. a-d), GeneNet (magenta, Fig. e-h), B-NW-SL (purple, Fig. i-l), D-S-NW-SL (cyan, Fig. m-p), and D-S-GL (orange, Fig. q-t), respectively. The lines correspond to the median AUC and the bands to the 25% and 75% percentiles of the distribution.

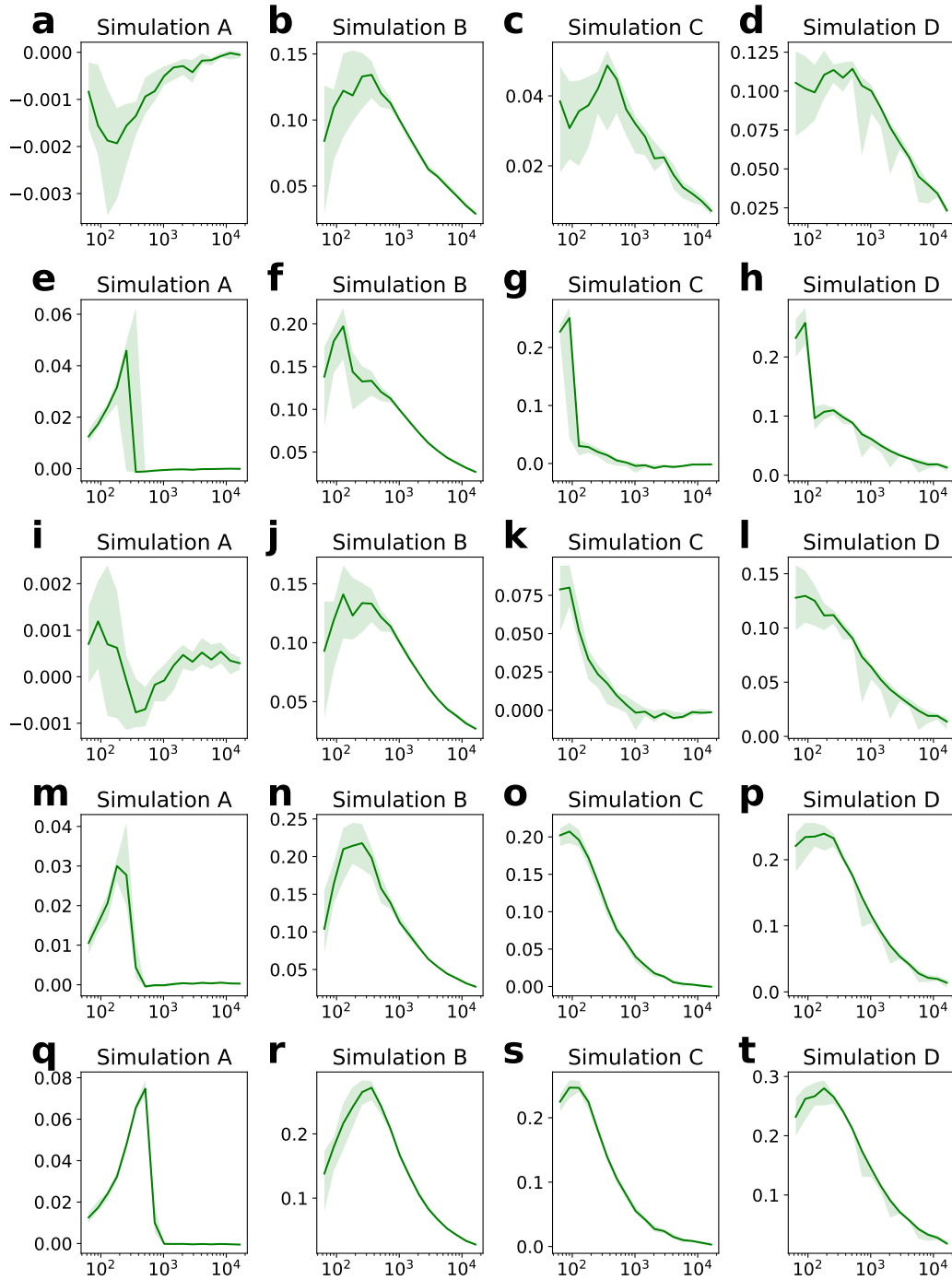


Figure 4: Area under the ROC curve (AUC) differences versus sample size n of simulation studies A to D (columns). Each row corresponds to the AUC difference DRAGON minus GGM (Fig. a-d), DRAGON minus GeneNet (Fig. e-h), DRAGON minus B-NW-SL (Fig. i-l), DRAGON minus D-S-NW-SL (Fig. m-p), and DRAGON minus D-S-GL (Fig. q-t), respectively. The green lines correspond to the median AUC and the bands to the 25% and 75% percentiles of the distribution.

3.2.1 Data acquisition, processing, and estimated DRAGON model

The GenomicDataCommons [32] R package, version 1.20.1, was used to download TCGA breast cancer data (Project ID TCGA-BRCA; dbGaP Study Accession phs000178) from the Genomic Data Commons.

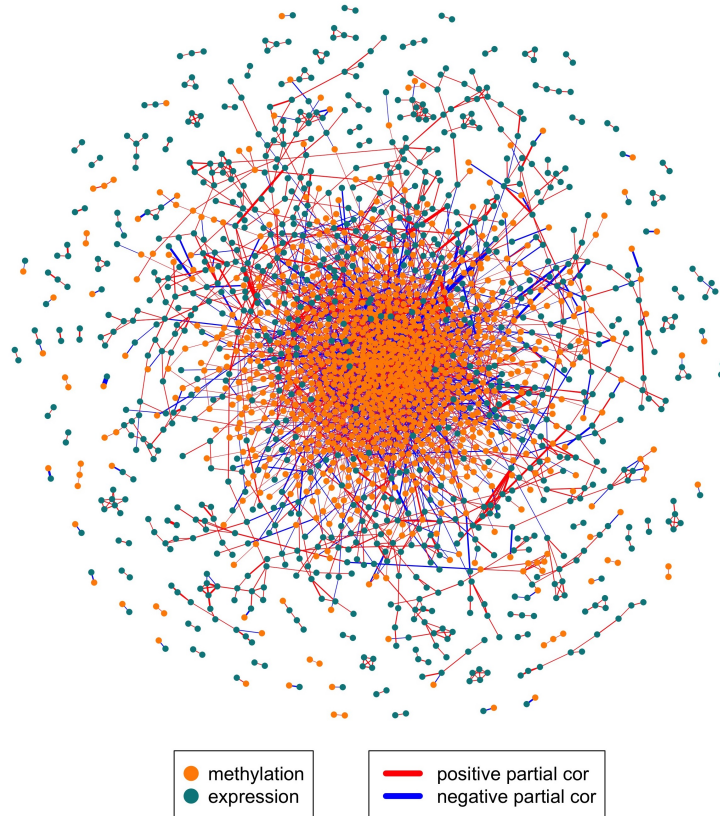


Figure 5: DRAGON multiomic network on TCGA methylation and gene expression data from 795 women with breast cancer.

Methylation levels from the Illumina 450k array were processed from raw data into beta values with the TCGA Methylation Array Harmonization Workflow [33], which uses SeSAMe [34] for signal detection and quality control. Methylation was summarized at the gene level by averaging beta values for probes in the promoter region of each gene of interest and methylation data were transformed to approximate normality with the nonparanormal transformation [35]. RNA-seq data were processed according to the TCGA RNA-Seq Alignment Workflow [36] to produce gene expression levels; this pipeline uses the Spliced Transcripts Alignment to a Reference (STAR) [37] algorithm to align reads and generate counts which were reported as Transcripts per Million (TPM), among other measures.

Methylation and expression data for the transcription factors for this breast cancer data set were loaded into DRAGON and a partial correlation network was calculated. A thresholded version of the DRAGON-estimated network consisting of all edges with $FDR < 0.005$ and all nodes with degree > 0 is shown in Figure 5. The network contains 3,631 edges on 2,106 nodes. 1,168 of the nodes represent methylation (75% of the methylation variables) and 938 represent gene expression (72 % of the gene expression variables).

3.2.2 DRAGON discovers meaningful promoter methylation-gene expression relationships

DNA methylation can regulate gene expression by blocking TF binding or by altering the binding of other regulatory proteins [38]. In cancer, hypermethylation of tumor suppressor gene promoters can lead to their inactivation by blocking transcription factors and inhibiting the recruitment of the transcriptional machinery [39]. On the other hand, DNA methylation results from the actions of proteins (methylases and demethylases) whose levels in turn result from changes in the expression of genes encoding these proteins. DRAGON provides a means to study both changes in gene expression resulting from methylation and the activation of methylation through changes in gene expression.

Because of the complex, correlated nature of methylation and gene expression, a multi-omic cor-

relation network based on these data may be too noisy to identify meaningful methylation-expression relationships. To illustrate this, we created a Pearson correlation network on the methylation-gene expression data with 825,256 significant methylation-gene expression edges based on the criteria $FDR < 0.05$. Notably, of these edges, only 862 (0.13%) were edges between the expression of a gene and the methylation of its promoter – the associations we expect functionally to be the most significant (175 (20%) positive and 687 (80%) negative edges). In contrast, when using DRAGON to estimate the partial correlation network on the same data, the result was a much sparser network consisting of 769 significant methylation-gene expression edges ($FDR < 0.05$). Of these edges, 333 (43%) were associations between expression of a gene and methylation of its promoter (26 (8%) positive and 307 (92%) negative partial correlations). The high proportion of negative partial correlations is an important “sanity check” on the performance of DRAGON, as promoter methylation suppresses transcription for most genes [39]. To further illustrate the discriminatory power of partial correlations relative to simple correlations, we examined the 769 most significant Pearson correlation edges between gene expression and methylation sites (corresponding to the number of gene expression-methylation edges in the DRAGON network) and found only 33 (4%) to be associations between expression of a gene and methylation of its promoter. Note that neither the Pearson correlation-based analysis nor the DRAGON analysis use any prior knowledge about methylation site - gene correspondence.

Returning to the DRAGON network, we ranked gene expression nodes according to the number of significant edges to methylation nodes they possessed (Table 3). The top-ranking gene, with 12 edges to methylation nodes (7 positive and 5 negative partial correlations), was ZFP57 (Fig. 6) which is a zinc finger transcription factor containing a KRAB domain and which may play a negative regulatory role [40]. The strongest gene expression - promoter methylation edge was observed between ZFP57 and methylation of its own promoter ($FDR < 10^{-100}$, $\rho = -0.25$), followed by methylation of the SKOR2 promoter ($FDR < 10^{-3}$, $\rho = -0.06$), and methylation of the ZNF121 promoter ($FDR < 10^{-3}$, $\rho = 0.06$). A comprehensive list of edges is shown in Table 3. ZFP57 is known to contribute in maintaining the methylation memory of parental origin [41]. It controls DNA methylation during the earliest multicellular developmental stages at multiple imprinting control regions [42, 43], which is in line with its multiple related methylation sites suggested by DRAGON. Most importantly, ZFP57 has been shown to suppress proliferation of breast cancer cells through down-regulation of the MEST-mediated Wnt/ β -catenin signalling pathway [44].

The second TF was ZNF334, another zinc finger protein transcription factor, which had 11 edges to methylation variables (4 positive, 7 negative; Fig. 6). Again, the strongest edge was observed to its own methylation site ($FDR < 10^{-34}$, $\rho = -0.1754$), followed by ZNF266 ($FDR = 3.6 \cdot 10^{-4}$, $\rho = -0.058$) and KLF2 ($FDR = 7.6 \cdot 10^{-4}$, $\rho = -0.056$). ZNF334 was recently identified as tumor suppressor of triple-negative breast cancer and higher ZNF334 expression was shown to be associated with better survival outcomes [45]. DRAGON suggests that this suppression may be due to hypermethylation of its promoter region. A similar pattern has been observed in some other cancers, including hepatocellular carcinoma [46].

The third and fourth top hits were the transcription factors NR6A1 (also known as GCNF) and MYRFL, both showing 10 edges to methylation variables (Supplementary Figure S16). Unlike the other transcription factors we identified, NR6A1 was not related to its own methylation site ($FDR \sim 1$, $\rho \sim 0$). Its strongest methylation-gene expression edges were observed to methylation sites attributed to the genes FOXO6 ($FDR < 1 \cdot 10^{-4}$, $\rho = 0.061$) and IKZF3 ($FDR < 1 \cdot 10^{-4}$, $\rho = 0.060$). FOXO6 is a transcription factor known to play multiple roles in breast cancer. Its downregulation is implicated in promotion of the epithelial-mesenchymal transition, in migration and proliferation of breast cancer cells, and in reduced cell resistance to the anti-cancer drug paclitaxel through the PI3K/Akt signaling pathway [47, 48]. IKZF3 is a member of the Ikaros family of zinc-finger proteins that has been shown to work with other transcription factors to regulate immune response in breast cancer [49] and its knockdown has been shown to dramatically increase breast cancer response to chimeric antigen receptor T-cell (CAR-T) therapy [50].

In *mus musculus*, NR6A1 has been shown to interact with DNMT3B (DNA (cytosine-5)-methyltransferase 3B) to induce promoter methylation of the genes Oct-3/4 [51]. DNMT3B together with DNMT3A is essential for the *de novo* methylation in early development [52]. In addition to its role as a transcription factor, NRA61 is an orphan nuclear receptor normally expressed in germ cells of gonads and highly expressed in triple-negative and ER + HER2 - breast cancer and so has been suggested as an ideal drug target [53]. MYRFL follows the more typical pattern, having its strongest methylation-gene expression

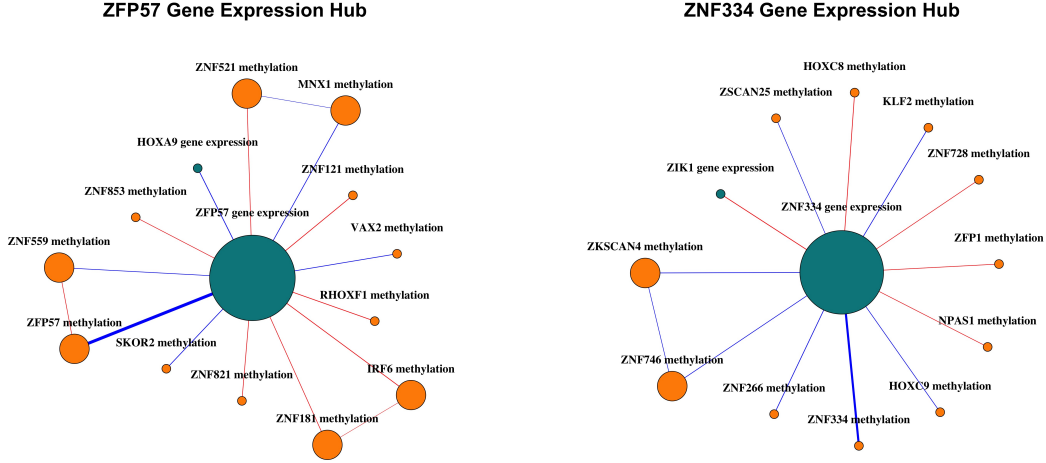


Figure 6: Neighborhoods of ZFP57 and ZNF334, two of the transcription factor gene expression nodes that serve as hubs in the DRAGON breast cancer network. Turquoise nodes represent gene expression and orange nodes represent promoter methylation. Red edges indicate positive partial correlations; blue, negative. Edge width is proportional to the strength of partial correlation. Larger nodes indicate higher node degrees. Edges with $FDR < 0.05$ are shown.

edge to its own methylation site ($FDR < 1 \cdot 10^{-7}$, $\rho = -0.073$). MYRFL encodes a transcription factor that is required for central nervous system myelination and it has been identified as a member of a regulatory cluster of genes on chromosome 12 that has been associated with elevated risk of breast cancer [54].

Although this analysis does not fully account for either the complexities of breast cancer and its subtypes or for the interplay of regulatory mechanisms active in cells and limited exploration to the transcription factors themselves, it already paints a compelling picture of the interplay between epigenetic regulation through altered patterns of methylation in breast cancer and activation or repression of key regulatory proteins that control breast cancer risk, cell proliferation, and response to various therapeutic interventions.

Table 3: Summary of the 4 gene-expression variables with most edges to methylation variables ordered by rank. Methylation variables (last column) are ordered by partial correlations (from high to low absolute values), where the $+/-$ signs in brackets give the signs of the estimated partial correlations.

rank	TF RNA	#GE-methyl. edges	methylation variables
1	ZFP57	12	ZFP57(-), SKOR2(-), ZNF121(+), IRF6(+), RHOXF1(+), MNX1(-), VAX2(-), ZNF821(+), ZNF181(+), ZNF559(-), ZNF521(+), ZNF853(+)
2	ZNF334	11	ZNF334(-), ZNF266(-), KLF2(-), ZKSCAN4(-), HOXC8(+), ZNF746(-), HOXC9(-), ZFP1(+), ZNF728(+), ZSCAN25(-), NPAS1(+)
3	NR6A1	10	FOXO6(+), IKZF3(+), JRK(-), NR5A1(+), NFIC(+), ZNF654(-), FOXR1(-), ETV2(+), ELK3(+), FOXP1(-)
4	MYRFL	10	MYRFL(-), ZFP69B(-), AHR(-), HOXB7(+), ZNF467(-), THAP12(+), ZNF251(-), MTF1(+), ARID5A(+), RORB(+)

3.2.3 Community detection and enrichment analysis

To further analyze the complex structure of the estimated network, we clustered nodes using community detection on the DRAGON-estimated network thresholded at $FDR < 0.005$. This threshold was based on inspection of the distribution of FDR-corrected p -values; Supplementary Figure S17. Community detection was performed using the `cluster_fast_greedy` algorithm as implemented in the `igraph` R

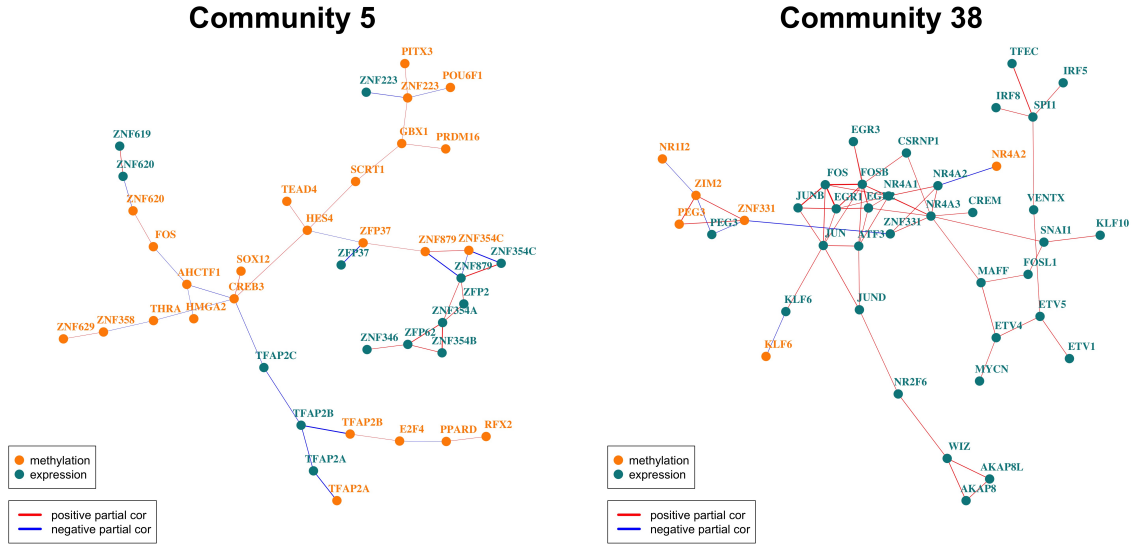


Figure 7: Example communities of interest in the DRAGON breast cancer gene expression-methylation network. Community 5 contains the TFAP2 family of transcription factors. Community 38 contains several hallmark cancer genes that are highly connected.

package [55, 56] (see Supplement). Using this algorithm, 169 communities were detected, 59 of which had at least 5 nodes.

To assess the enrichment of methylation-gene expression communities for functions potentially related to breast cancer, we performed an over-representation analysis (ORA) for Reactome gene sets [57] within each of the 59 communities with at least 5 nodes (for details of the ORA, see Supplement). The `fora` function of the `fgsea` R package was used to conduct the ORA [58]. Reactome gene sets with at least 3 genes were considered (`minSize = 3`). For the analysis presented here, it should be noted that each transcription factor gene may appear twice, once based on its expression and once based on its methylation. Therefore, the universe of possible genes considered for the ORA (and used to set background expectations) is twice the size of the number of TFs included in the DRAGON model. We also performed an ORA assessing enrichment for methylation only and one assessing enrichment for expression only. A Reactome pathway was identified as over-represented in a community if its FDR was less than 0.05 in at least one of these three ORAs (Benjamini-Hochberg FDR as implemented in `fgsea`). Ten of the 59 communities of size ≥ 5 genes were enriched for at least one REACTOME pathway at FDR < 0.05 ; complete results of the enrichment analysis are available in Supplementary Data 1. Here, we highlight two communities that illustrate DRAGON’s ability to provide unexpected insight into disease processes.

Community 5 consists of 39 TF nodes, 14 based on TF gene expression and 25 based on TF promoter methylation (Figure 7). The TF set in community 5 is enriched for several Reactome pathways related to the TFAP2 family of transcription factors (Supplementary Data 1). TFAP2C has been implicated in estrogen response signaling in breast cancer, which plays a major role in breast cancer development, progression, and therapeutic response[59]; estrogen response signaling is also a key determinant of breast cancer molecular subtype [60].

To explore the role of the TFAP2 family in our DRAGON network, we obtained mRNA-based subtype classifications (basal, HER2, luminal A, luminal B, and normal) for the tumor samples using the `PanCancerAtlas_subtypes` function from the `TCGAbioLinks` R package [61]. We then evaluated subtype-specific methylation and expression among the TFAP2 genes represented in Community 5 (TFAP2A methylation and expression, TFAP2B methylation and expression, TFAP2C expression; Supplementary Figure S18).

TFAP2A and TFAP2B methylation both differed significantly based on subtype (Kruskal-Wallis test, TFAP2A $p = 3.3 \cdot 10^{-4}$; TFAP2B $p < 1 \cdot 10^{-15}$) as did TFAP2A, TFAP2B, and TFAP2C expression

(TFAP2A $p = 1.9 \cdot 10^{-12}$, TFAP2B $p < 1 \cdot 10^{-15}$, TFAP2C $p < 1.9 \cdot 10^{-10}$). However, TFAP2C methylation, which was notably excluded from this community, did not differ significantly between subtypes ($p = 0.17$). To illustrate the multi-omic phenotyping possible with DRAGON communities, we investigated TFAP2B further. The median TFAP2B promoter methylation beta level was 0.55 in basal samples versus 0.17 in non-basal samples; the median TFAP2B expression among basal samples was 0.49 TPM vs. a median of 36.46 TPM in non-basal samples. This multi-omic phenotype of increased methylation and decreased expression in basal samples follows the canonical paradigm that promoter methylation results in gene silencing. To explore the predictive power of this joint information, we constructed a logistic regression model for multi-omic subtype classification, regressing basal vs. non-basal subtype against TFAP2B methylation, expression, and an interaction term between the two. In the resulting model, TFAP2B methylation and the interaction term between TFAP2B methylation and expression were both significant (methylation: OR = 147.76, 95 % CI: [44.21, 493.82]; methylation*expression: OR = 0.873, 95 % CI: [0.797, 0.957]) while TFAP2B expression was not (OR = 1.004, 95 % CI: [0.989, 1.018]). The AUROC of this model was 0.85; in contrast, the AUROC of a similar model using TFAP2B methylation alone as a predictor was 0.82 and using TFAP2B expression alone, 0.79, demonstrating the synergistic power of multi-omic features for class discrimination. Although this classification model does not outperform the expression-based subtype classification used by the TCGA, these results are nonetheless impressive given that they are based on two measurements of the omic state of a single gene.

Community 38 consists of 40 nodes, six of which represent promoter methylation and 34 of which represent gene expression (Figure 7). This community is enriched for 21 Reactome pathways, including signaling by receptor tyrosine kinases (FDR = $4.7 \cdot 10^{-9}$), estrogen-dependent gene expression (FDR = $1.5 \cdot 10^{-3}$), PTEN regulation (FDR = 0.02), and MAPK family signaling cascades (FDR = 0.02). The nodes primarily driving these enrichments include EGR1, EGR2, EGR3, FOS, FOSB, JUNB, and JUND. These seven nodes comprise a tightly co-expressed subgraph of Community 38 and are well-known players in cancer signaling [62, 63].

NR4A2 methylation and KLF6 methylation are both degree-one nodes in Community 38; their only edges indicate negative partial correlation with their own expression. It may be that differential methylation of NR4A2 and KLF6 drives subtype-specific activity in the pathways of this community by modulating the expression of NR4A2 and KLF6, which are connected via FOS and JUN expression to the eight-node cluster of coexpressed TFs. In comparing these nodes between subtypes, we found that both KLF6 and NR4A2 are significantly differentially methylated (KLF6: Kruskal-Wallis chi-squared = 93.04, df = 4, $p < 2.2 \cdot 10^{-16}$; NR4A2: Kruskal-Wallis chi-squared = 17.98, df = 4, $p = 0.001$; Supplementary Figure S21). To provide a benchmark for differential methylation between subtypes, we performed the same statistical test for a “housekeeping” transcription factor (ATF1), which showed no significant difference in methylation (Kruskal-Wallis chi-squared = 6.62, df = 4, $p = 0.158$; Supplementary Figure S19), indicating that the differential methylation of these key transcription factors may play a substantial role in breast cancer beyond those already discussed, particularly given their association with the EGR/FOS/JUN expression cluster and the importance of these transcription factors in a wide range of cancer processes.

4 Conclusion and Summary

Regulation of transcriptional processes in the cell involve multiple interacting partners that include transcription factors and their expression, regulation of their targets, and epigenetic factors such as DNA methylation that may enhance or disrupt regulatory interactions. Simple measures such as correlation fail to capture meaningful regulatory associations and can be dominated by spurious correlations between genes that are expressed at relatively low levels or that exhibit similar patterns of expression due to factors unrelated to the biological state of the system. Partial correlation analysis allows better discrimination between potentially causal associations between regulators and their regulatory targets and may lead to greater insight into the underlying biology of the systems we choose to study. The problem in conducting such an analysis is that different types of omics data often present with different scales, biases, and error distributions.

DRAGON is a partial correlation framework optimized for the integration of multiple “layers” of omics data into a unified association network that allows us to understand both associations between biological variables such as gene expression and the potential drivers of the observed correlations. DRAGON is

based on Gaussian Graphical Models (GGMs) and uses a regularization scheme to optimize the trade-off between the network’s complexity and its estimation accuracy while explicitly taking into account the distinct data characteristics of the various omics data types used in the model. DRAGON accounts for differences in edge densities and feature sizes, enabling improved estimation of partial correlations compared to layer-agnostic GGMs. The advantages of DRAGON are particularly evident in simulations when the number of variables p is the same order of magnitude or exceeds the sample size n , as is the case in nearly all omics experiments.

We recognize that DRAGON has some limitations. DRAGON’s GGM framework assumes multivariate normally distributed data which, for biological data, generally does not hold. For continuous distributions, data transformations such as the nonparanormal transformation [35] can be used to adjust input data to be approximately normally distributed; this approach, for example, allowed us to use DRAGON with methylation and gene expression data. However, other omics data types such as single-nucleotide polymorphism (SNP) data are categorical or ordinal, and alternative methods are needed to build these important regulatory elements into the DRAGON framework. Extending DRAGON to Mixed Graphical Models [64, 65], which incorporate both continuous and discrete variables, could allow us to overcome this limitation of the current implementation.

It is also worth noting that DRAGON does not incorporate pre-defined network structures. Structured probabilistic graphical models have been studied fairly extensively [66, 67, 68, 69] as they allow users to bias networks towards a given structure consistent with biological prior knowledge. Work by our group and others has demonstrated the power of introducing soft, knowledge-based constraints into optimization problems such as gene regulatory network inference [70, 5]. In the case of DRAGON, this could be achieved by *a priori* removing edges from the model based on known regulatory relationships by, for example, estimating the inverse biased covariance matrix with *a priori* specified zero entries [71]. Alternatively, one could construct a model in which “established” associations between elements are more likely to be included into the network by shifting their weights at initiation [67] or through the use of modified target matrices $T^{(k)}$ in Eq. (3). Both approaches, alone or in combination, would need to be carefully tested taking into account the effect that a bias on the network structure has on estimates of significance levels.

Although DRAGON represents an important step forward given our ability to collect increasingly large, multi-omic data sets, it is important to recognize that many problems in network inference are not addressed by DRAGON. Partial correlation relies on the data we have available, and many regulatory data types simply cannot be collected simultaneously and so remain hidden. Such hidden variables can lead to spurious associations and hamper the interpretation of networks in general. New technologies may provide additional omics layers, but integration of these will require additional methodological advances and the development of robust and scalable computational models.

Second, conditional independence is only one way to model associations in biological data. Conditional independence relationships encode the factorization properties of probability distributions and while appealing as a model, it is difficult to state definitively how this concept maps to the complexity of regulatory processes in biological systems. However, the same limitation holds for all measures of “relatedness,” comprising mutual exclusivity [9] and multivariate information measures [72]. Elucidation of which type of similarity measure is most appropriate for inference of networks from biological data remains an open challenge [73], but probabilistic graphical models have been shown to perform well relative to other approaches (see the lasso regression methods in [73] as an example). To give a clear answer, experimental data together with the corresponding ground truth is optimally needed, but our use of inference methods underlies our present inability to determine the true regulatory processes that drive biological states. Consequently, method comparison of probabilistic graphical models that allows us to specify appropriate benchmarks with respect to edge recovery, maximum likelihood, and false discovery rate are the best available methods for testing the basic process of network inference and modeling, and assessment of biological insight gained through model analysis remains a key element of validating new methods. On both accounts, DRAGON performs well giving limited data sets that reflect those typically available in omics studies of human health and disease. We also note that our analysis focused on observational data only, and the inferred networks are undirected. Statements on causality from observational data are difficult given correlation-based models, although it is possible to provide lower bounds on causal effects [74]. However, our biological understanding of cause and effect can guide us, at least in part. Nevertheless, additional work needs to be done to address causality in the context of multi-omics and the use of structured approaches that incorporate prior causal knowledge may be an

important next step. A simple adherence to the “central dogma of molecular biology,” that DNA makes RNA, and RNA makes protein, could assist in defining causal relationships. Importantly, specifying a prior belief should not prohibit the inference of more complex regulatory mechanisms contradicting these beliefs: otherwise, we stand to discover only what we already know.

DRAGON represents a significant contribution to network inference by presenting a framework for modeling of partial correlations across multiple layers of omics data. DRAGON-estimated networks provide new insights into regulatory processes that may be overlooked by other methods as they are capable of identifying direct multi-omic relationships via a Gaussian graphical model framework. DRAGON is easy to use and freely available as open source software in the Network Zoo package (netZooPy v0.8; netzoo.github.io).

5 Code and data availability

DRAGON is available through the Network Zoo package (netZooPy v0.8; netzoo.github.io) and a vignette to demonstrate its use can be found in netBooks (netbooks.networkmedicine.org). Code to reproduce the TCGA breast cancer methylation analysis is available on Github at <https://github.com/katehoffshutta/DRAGON-TCGA-BRCA>.

6 Support

KHS was supported by grant 2T32HL007427 from the National Heart, Lung, and Blood Institute of the US National Institutes of Health. DW, RB, MBG, JQ, and MA were supported by grants from the US National Cancer Institute (1R35CA220523 and 1U24CA231846). DLD was supported by grants from the US National Institutes of Health, award numbers R01HG011393 and P01114501. The work of HUZ and MA was supported by the German Federal Ministry of Education and Research (BMBF) within the framework of the e:Med research and funding concept (grant no. 01ZX1912A and 01ZX1912C).

7 Acknowledgments

The results shown here are in whole or part based upon data generated by the TCGA Research Network: <https://www.cancer.gov/tcga>.

References

- [1] Ulrich Stelzl, Uwe Worm, Maciej Lalowski, Christian Haenig, Felix H Brembeck, Heike Goehler, Martin Stroedicke, Martina Zenkner, Anke Schoenherr, Susanne Koeppen, et al. A human protein-protein interaction network: a resource for annotating the proteome. *Cell*, 122(6):957–968, 2005.
- [2] Jean-François Rual, Kavitha Venkatesan, Tong Hao, Tomoko Hirozane-Kishikawa, Amélie Dricot, Ning Li, Gabriel F Berriz, Francis D Gibbons, Matija Dreze, Nono Ayivi-Guedehoussou, et al. Towards a proteome-scale map of the human protein-protein interaction network. *Nature*, 437(7062):1173–1178, 2005.
- [3] Damian Szklarczyk, Annika L Gable, David Lyon, Alexander Junge, Stefan Wyder, Jaime Huerta-Cepas, Milan Simonovic, Nadezhda T Doncheva, John H Morris, Peer Bork, et al. String v11: protein-protein association networks with increased coverage, supporting functional discovery in genome-wide experimental datasets. *Nucleic acids research*, 47(D1):D607–D613, 2019.
- [4] Florian Markowetz and Rainer Spang. Inferring cellular networks—a review. *BMC bioinformatics*, 8(6):S5, 2007.
- [5] Kimberly Glass, Curtis Huttenhower, John Quackenbush, and Guo-Cheng Yuan. Passing messages between biological networks to refine predicted interactions. *PloS one*, 8(5), 2013.

- [6] Koh Aoki, Yoshiyuki Ogata, and Daisuke Shibata. Approaches for extracting practical information from gene co-expression networks in plant biology. *Plant and Cell Physiology*, 48(3):381–390, 2007.
- [7] Michael Altenbuchinger, Antoine Weihs, John Quackenbush, Hans Jürgen Grabe, and Helena U Zacharias. Gaussian and mixed graphical models as (multi-) omics data analysis tools. *Biochimica et Biophysica Acta (BBA)-Gene Regulatory Mechanisms*, 1863(6):194418, 2020.
- [8] John Aldrich et al. Correlations genuine and spurious in pearson and yule. *Statistical science*, 10(4):364–376, 1995.
- [9] Adam A Margolin, Ilya Nemenman, Katia Basso, Chris Wiggins, Gustavo Stolovitzky, Riccardo Dalla Favera, and Andrea Califano. Aracne: an algorithm for the reconstruction of gene regulatory networks in a mammalian cellular context. In *BMC bioinformatics*, volume 7, pages 1–15. BioMed Central, 2006.
- [10] Atul J Butte and Isaac S Kohane. Mutual information relevance networks: functional genomic clustering using pairwise entropy measurements. In *Biocomputing 2000*, pages 418–429. World Scientific, 1999.
- [11] Anja Wille, Philip Zimmermann, Eva Vranová, Andreas Fürholz, Oliver Laule, Stefan Bleuler, Lars Hennig, Amela Prelić, Peter von Rohr, Lothar Thiele, et al. Sparse graphical gaussian modeling of the isoprenoid gene network in arabidopsis thaliana. *Genome biology*, 5(11):R92, 2004.
- [12] Juliane Schäfer and Korbinian Strimmer. A shrinkage approach to large-scale covariance matrix estimation and implications for functional genomics. *Statistical applications in genetics and molecular biology*, 4(1), 2005.
- [13] Jan Krumsiek, Karsten Suhre, Thomas Illig, Jerzy Adamski, and Fabian J Theis. Gaussian graphical modeling reconstructs pathway reactions from high-throughput metabolomics data. *BMC systems biology*, 5(1):21, 2011.
- [14] Mahsa Ghanbari, Julia Lasserre, and Martin Vingron. The distance precision matrix: computing networks from non-linear relationships. *Bioinformatics*, 35(6):1009–1017, 2019.
- [15] Junyue Cao, Darren A Cusanovich, Vijay Ramani, Delasa Aghamirzaie, Hannah A Pliner, Andrew J Hill, Riza M Daza, Jose L McFaline-Figueroa, Jonathan S Packer, Lena Christiansen, et al. Joint profiling of chromatin accessibility and gene expression in thousands of single cells. *Science*, 361(6409):1380–1385, 2018.
- [16] Nicolai Meinshausen, Peter Bühlmann, et al. High-dimensional graphs and variable selection with the lasso. *The annals of statistics*, 34(3):1436–1462, 2006.
- [17] Jerome Friedman, Trevor Hastie, and Robert Tibshirani. Sparse inverse covariance estimation with the graphical lasso. *Biostatistics*, 9(3):432–441, 2008.
- [18] Steffen L Lauritzen. *Graphical models*, volume 17. Clarendon Press, 1996.
- [19] Christopher M Bishop. *Pattern recognition and machine learning*. springer, 2006.
- [20] Olivier Ledoit and Michael Wolf. A well conditioned estimator for large dimensional covariance matrices. 2000.
- [21] Victor Bernal, Rainer Bischoff, Victor Guryev, Marco Grzegorzcyk, and Peter Horvatovich. Exact hypothesis testing for shrinkage-based gaussian graphical models. *Bioinformatics*, 35(23):5011–5017, 2019.
- [22] Yoav Benjamini and Yosef Hochberg. Controlling the false discovery rate: a practical and powerful approach to multiple testing. *Journal of the Royal statistical society: series B (Methodological)*, 57(1):289–300, 1995.
- [23] Juliane Schaefer, Rainer Opgen-Rhein, and Korbinian Strimmer. *GeneNet: Modeling and Inferring Gene Networks*, 2020. R package version 1.2.15.

- [24] Juliane Schäfer and Korbinian Strimmer. An empirical bayes approach to inferring large-scale gene association networks. *Bioinformatics*, 21(6):754–764, 2005.
- [25] Zhao Ren, Tingni Sun, Cun-Hui Zhang, and Harrison H Zhou. Asymptotic normality and optimality in estimation of large gaussian graphical models. *The Annals of Statistics*, 43(3):991–1026, 2015.
- [26] Rong Zhang, Zhao Ren, and Wei Chen. Silggm: An extensive r package for efficient statistical inference in large-scale gene networks. *PLoS computational biology*, 14(8):e1006369, 2018.
- [27] Jana Janková and Sara van de Geer. Honest confidence regions and optimality in high-dimensional precision matrix estimation. *Test*, 26(1):143–162, 2017.
- [28] Jana Jankova and Sara Van De Geer. Confidence intervals for high-dimensional inverse covariance estimation. *Electronic Journal of Statistics*, 9(1):1205–1229, 2015.
- [29] Wei-Yun Huang, Sheng-Da Hsu, Hsi-Yuan Huang, Yi-Ming Sun, Chih-Hung Chou, Shun-Long Weng, and Hsien-Da Huang. MethHC: a database of DNA methylation and gene expression in human cancer. *Nucleic Acids Research*, 43(D1):D856–D861, 11 2014.
- [30] Katarzyna Tomczak, Patrycja Czerwińska, and Maciej Wiznerowicz. The cancer genome atlas (tcga): an immeasurable source of knowledge. *Contemporary oncology*, 19(1A):A68, 2015.
- [31] Samuel A Lambert, Arttu Jolma, Laura F Campitelli, Pratyush K Das, Yimeng Yin, Mihai Albu, Xiaoting Chen, Jussi Taipale, Timothy R Hughes, and Matthew T Weirauch. The human transcription factors. *Cell*, 172(4):650–665, 2018.
- [32] Robert L Grossman, Allison P Heath, Vincent Ferretti, Harold E Varmus, Douglas R Lowy, Warren A Kibbe, and Louis M Staudt. Toward a shared vision for cancer genomic data. *New England Journal of Medicine*, 375(12):1109–1112, 2016.
- [33] Tcga methylation array harmonization workflow. Accessed: 2022-05-25.
- [34] Wanding Zhou, Timothy J Triche Jr, Peter W Laird, and Hui Shen. Sesame: reducing artifactual detection of dna methylation by infinium beadchips in genomic deletions. *Nucleic acids research*, 46(20):e123–e123, 2018.
- [35] Han Liu, John Lafferty, and Larry Wasserman. The nonparanormal: Semiparametric estimation of high dimensional undirected graphs. *Journal of Machine Learning Research*, 10(Oct):2295–2328, 2009.
- [36] Tcga mrna analysis pipeline. Accessed: 2022-05-25.
- [37] Alexander Dobin, Carrie A Davis, Felix Schlesinger, Jorg Drenkow, Chris Zaleski, Sonali Jha, Philippe Batut, Mark Chaisson, and Thomas R Gingeras. Star: ultrafast universal rna-seq aligner. *Bioinformatics*, 29(1):15–21, 2013.
- [38] Lisa D Moore, Thuc Le, and Guoping Fan. Dna methylation and its basic function. *Neuropsychopharmacology*, 38(1):23–38, 2013.
- [39] Marta Kulis and Manel Esteller. 2 - dna methylation and cancer. In Zdenko Herceg and Toshikazu Ushijima, editors, *Epigenetics and Cancer, Part A*, volume 70 of *Advances in Genetics*, pages 27–56. Academic Press, 2010.
- [40] Ryutaro Hirasawa and Robert Feil. A krab domain zinc finger protein in imprinting and disease. *Developmental cell*, 15(4):487–488, 2008.
- [41] Hui Shi, Ruslan Strogantsev, Nozomi Takahashi, Anastasiya Kazachenka, Matthew C Lorincz, Myriam Hemberger, and Anne C Ferguson-Smith. Zfp57 regulation of transposable elements and gene expression within and beyond imprinted domains. *Epigenetics & chromatin*, 12(1):1–13, 2019.

- [42] Deborah JG Mackay, Jonathan LA Callaway, Sophie M Marks, Helen E White, Carlo L Acerini, Susanne E Boonen, Pinar Dayanikli, Helen V Firth, Judith A Goodship, Andreas P Haemers, et al. Hypomethylation of multiple imprinted loci in individuals with transient neonatal diabetes is associated with mutations in *zfp57*. Nature genetics, 40(8):949–951, 2008.
- [43] Nozomi Takahashi, Andrea Coluccio, Christian W Thorball, Evarist Planet, Hui Shi, Sandra Offner, Priscilla Turelli, Michael Imbeault, Anne C Ferguson-Smith, and Didier Trono. *Znf445* is a primary regulator of genomic imprinting. Genes & development, 33(1-2):49–54, 2019.
- [44] Lie Chen, Xiaowei Wu, Hui Xie, Na Yao, Yiqin Xia, Ge Ma, Mengjia Qian, Han Ge, Yangyang Cui, Yue Huang, et al. *Zfp57* suppress proliferation of breast cancer cells through down-regulation of mest-mediated wnt/ β -catenin signalling pathway. Cell death & disease, 10(3):1–15, 2019.
- [45] Zhaobo Cheng, Renjie Yu, Li Li, Junhao Mu, Yijia Gong, Fan Wu, Yujia Liu, Xiangyi Zhou, Xiaohua Zeng, Yongzhong Wu, et al. Disruption of *znf334* promotes triple-negative breast carcinoma malignancy through the *sfrp1/wnt/ β -catenin* signaling axis. Cellular and Molecular Life Sciences, 79(5):1–17, 2022.
- [46] Dapeng Sun, Xiaojie Gan, Lei Liu, Yuan Yang, Dongyang Ding, Wen Li, Junyao Jiang, Wenbin Ding, Linghao Zhao, Guojun Hou, et al. Dna hypermethylation modification promotes the development of hepatocellular carcinoma by depressing the tumor suppressor gene *znf334*. Cell death & disease, 13(5):1–12, 2022.
- [47] Hui Ye and Meiling Duan. Downregulation of *foxo6* in breast cancer promotes epithelial–mesenchymal transition and facilitates migration and proliferation of cancer cells. Cancer management and research, 10:5145, 2018.
- [48] Xixiang Yu, Xixi Gao, Xiaoping Mao, Zhenjing Shi, Bangxuan Zhu, Linqin Xie, Shaodan Di, and Limin Jin. Knockdown of *foxo6* inhibits glycolysis and reduces cell resistance to paclitaxel in hcc cells via pi3k/akt signaling pathway. OncoTargets and therapy, 13:1545, 2020.
- [49] WA Da Silveira, PVB Palma, RD Sicchieri, Rolando AR Villacis, LRM Mandarano, TMG Oliveira, HMR Antonio, Jurandyr Moreira de Andrade, Valdair Francisco Muglia, SR Rogatto, et al. Transcription factor networks derived from breast cancer stem cells control the immune response in the basal subtype. Scientific reports, 7(1):1–13, 2017.
- [50] Yan Zou, Bo Liu, Long Li, Qinan Yin, Jiaying Tang, Zhengyu Jing, Xingxu Huang, Xuekai Zhu, and Tian Chi. *Ikzf3* deficiency potentiates chimeric antigen receptor t cells targeting solid tumors. Cancer Letters, 524:121–130, 2022.
- [51] Noriko Sato, Mitsumasa Kondo, and Ken-ichi Arai. The orphan nuclear receptor *gcnf* recruits dna methyltransferase for *oct-3/4* silencing. Biochemical and biophysical research communications, 344(3):845–851, 2006.
- [52] Masaki Okano, Daphne W Bell, Daniel A Haber, and En Li. Dna methyltransferases *dnmt3a* and *dnmt3b* are essential for de novo methylation and mammalian development. Cell, 99(3):247–257, 1999.
- [53] Scooter Willis, Pradip De, Nandini Dey, Bradley Long, Brandon Young, Joseph A Sparano, Victoria Wang, Nancy E Davidson, and Brian R Leyland-Jones. Enriched transcription factor signatures in triple negative breast cancer indicates possible targeted therapies with existing drugs. Meta gene, 4:129–141, 2015.
- [54] Michael J Madsen, Stacey Knight, Carol Sweeney, Rachel Factor, Mohamed Salama, Inge J Stijleman, Venkatesh Rajamanickam, Bryan E Welm, Sasi Arunachalam, Brandt Jones, et al. Reparameterization of *pam50* expression identifies novel breast tumor dimensions and leads to discovery of a genome-wide significant breast cancer locus at 12q15. Cancer Epidemiology, Biomarkers & Prevention, 27(6):644–652, 2018.
- [55] Pascal Pons and Matthieu Latapy. Computing communities in large networks using random walks. In International symposium on computer and information sciences, pages 284–293. Springer, 2005.

- [56] Gabor Csardi, Tamas Nepusz, et al. The igraph software package for complex network research. InterJournal, complex systems, 1695(5):1–9, 2006.
- [57] Marc Gillespie, Bijay Jassal, Ralf Stephan, Marija Milacic, Karen Rothfels, Andrea Senff-Ribeiro, Johannes Griss, Cristoffer Sevilla, Lisa Matthews, Chuqiao Gong, et al. The reactome pathway knowledgebase 2022. Nucleic acids research, 50(D1):D687–D692, 2022.
- [58] Gennady Korotkevich, Vladimir Sukhov, Nikolay Budin, Boris Shpak, Maxim N Artyomov, and Alexey Sergushichev. Fast gene set enrichment analysis. BioRxiv, page 060012, 2021.
- [59] George W Woodfield, Annamarie D Horan, Yizhen Chen, and Ronald J Weigel. Tfp2c controls hormone response in breast cancer cells through multiple pathways of estrogen signaling. Cancer research, 67(18):8439–8443, 2007.
- [60] Pilar Eroles, Ana Bosch, J Alejandro Pérez-Fidalgo, and Ana Lluch. Molecular biology in breast cancer: intrinsic subtypes and signaling pathways. Cancer treatment reviews, 38(6):698–707, 2012.
- [61] Antonio Colaprico, Tiago C Silva, Catharina Olsen, Luciano Garofano, Claudia Cava, Davide Garolini, Thais S Sabedot, Tathiane M Malta, Stefano M Pagnotta, Isabella Castiglioni, et al. Tc-gabiolinks: an r/bioconductor package for integrative analysis of tcga data. Nucleic acids research, 44(8):e71–e71, 2016.
- [62] Adrian V Lee, Xiaojiang Cui, and Steffi Oesterreich. Cross-talk among estrogen receptor, epidermal growth factor, and insulin-like growth factor signaling in breast cancer. Clinical Cancer Research, 7(12):4429s–4435s, 2001.
- [63] Bin Wang, Hanfei Guo, Hongquan Yu, Yong Chen, Haiyang Xu, and Gang Zhao. The role of the transcription factor egr1 in cancer. Frontiers in Oncology, 11:775, 2021.
- [64] Jason D Lee and Trevor J Hastie. Learning the structure of mixed graphical models. Journal of Computational and Graphical Statistics, 24(1):230–253, 2015.
- [65] Michael Altenbuchinger, Helena U Zacharias, Stefan Solbrig, Andreas Schäfer, Mustafa Büyüközkan, Ulla T Schultheiß, Fruzsina Kotsis, Anna Köttgen, Rainer Spang, Peter J Oefner, et al. A multi-source data integration approach reveals novel associations between metabolites and renal outcomes in the german chronic kidney disease study. Scientific reports, 9(1):1–13, 2019.
- [66] Christophe Ambroise, Julien Chiquet, and Catherine Matias. Inferring sparse gaussian graphical models with latent structure. Electronic Journal of Statistics, 3:205–238, 2009.
- [67] Jing Ma, Ali Shojaie, and George Michailidis. Network-based pathway enrichment analysis with incomplete network information. Bioinformatics, 32(20):3165–3174, 2016.
- [68] Alireza F Siahpirani and Sushmita Roy. A prior-based integrative framework for functional transcriptional regulatory network inference. Nucleic acids research, 45(4):e21–e21, 2017.
- [69] Yonghua Zhuang, Fuyong Xing, Debashis Ghosh, Farnoush Banaei-Kashani, Russell P Bowler, and Katerina Kechris. An augmented high-dimensional graphical lasso method to incorporate prior biological knowledge for global network learning. Frontiers in genetics, page 2405, 2022.
- [70] David H Wolpert and William G Macready. No free lunch theorems for optimization. IEEE transactions on evolutionary computation, 1(1):67–82, 1997.
- [71] Trevor Hastie, Robert Tibshirani, Jerome H Friedman, and Jerome H Friedman. The elements of statistical learning: data mining, inference, and prediction, volume 2. Springer, 2009.
- [72] Thalia E Chan, Michael PH Stumpf, and Ann C Babbie. Gene regulatory network inference from single-cell data using multivariate information measures. Cell systems, 5(3):251–267, 2017.
- [73] Daniel Marbach, James C Costello, Robert Küffner, Nicole M Vega, Robert J Prill, Diogo M Camacho, Kyle R Allison, Manolis Kellis, James J Collins, and Gustavo Stolovitzky. Wisdom of crowds for robust gene network inference. Nature methods, 9(8):796–804, 2012.

- [74] Marloes H Maathuis, Diego Colombo, Markus Kalisch, and Peter Bühlmann. Predicting causal effects in large-scale systems from observational data. Nature methods, 7(4):247–248, 2010.

Supplementary Material

DRAGON: Determining Regulatory Associations using Graphical models on multi-Omic Networks

1. Analytical estimates for regularization parameters λ_1 and λ_2

Equation 8 of the main manuscript decomposes the quantity

$$R = E [||\hat{\Sigma} - \Sigma||_F^2] \quad (1)$$

into terms which can be efficiently calculated analytically, yielding estimates for optimal regularization parameters λ_1 and λ_2 of DRAGON in the 2-omic case. Here, we derive this equation.

Notation

Let $\Sigma = \{\sigma_{ij}\}$ be the true population covariance and let $S = \{s_{ij}\}$ be sample covariance, i.e., the usual maximum likelihood estimator for Σ . Next, let $\hat{\Sigma} = \{\hat{\sigma}_{ij}\}$ be the covariance shrinkage estimator defined in the main manuscript, i.e.:

$$\hat{\Sigma} = \{\hat{\sigma}_{ij}\} = \begin{pmatrix} (1 - \lambda_1)S^{(1,1)} & \sqrt{1 - \lambda_1}\sqrt{1 - \lambda_2}S^{(1,2)} \\ \sqrt{1 - \lambda_2}\sqrt{1 - \lambda_1}S^{(2,1)} & (1 - \lambda_2)S^{(2,2)} \end{pmatrix} + \begin{pmatrix} \lambda_1 \text{diag}(S^{(1,1)}) & 0 \\ 0 & \lambda_2 \text{diag}(S^{(2,2)}) \end{pmatrix} \quad (2)$$

where we have divided S into blocks consisting of $S^{(1,1)}$, the sample covariance of omics layer 1; $S^{(2,2)}$, the sample covariance of omics layer 2; and $S^{(1,2)} = t(S^{(2,1)})$, the sample covariance between omics layer 1 and omics layer 2. Finally, let $(i, j)^{(A,B)}$ represent the row and column indices in the (A, B) block of the matrices Σ and S .

Derivation

We derive an expression for R in terms of λ_1 and λ_2 by considering three cases:

- (i) i, j such that σ_{ij} represents the within-omic covariance of two variables i and j , both in omics layer 1. The notation we use for these indices is $(i, j)^{(1,1)}$.
- (ii) i, j such that σ_{ij} represents the within-omic covariance of two variables i and j , both in omics layer 2. The notation we use for these indices is $(i, j)^{(2,2)}$.
- (iii) i, j such that σ_{ij} represents the between-omic covariance of variable i , which is in omics layer 1, and variable j , which is in omics layer 2. The notation we use for these indices is $(i, j)^{(1,2)}$.

In deriving these steps, we partition R into the sum of four components: $R^{(1,1)}$, obtained from $\Sigma^{(1,1)}$ and $S^{(1,1)}$; $R^{(2,2)}$, obtained from $\Sigma^{(2,2)}$ and $S^{(2,2)}$; $R^{(1,2)}$, obtained from $\Sigma^{(1,2)}$ and $S^{(1,2)}$; and $R^{(2,1)}$, obtained from $\Sigma^{(2,1)}$ and $S^{(2,1)}$. From these, we can write the final equation

$$\begin{aligned} R &= R^{(1,1)} + R^{(2,2)} + R^{(1,2)} + R^{(2,1)} \\ &= R^{(1,1)} + R^{(2,2)} + 2R^{(1,2)} \end{aligned}$$

where the last line arises due to the symmetric nature of the covariance matrix and the Frobenius norm.

Case (i): both variables in omics layer 1

In this case, we have

$$\begin{aligned}
 R^{(1,1)} &= E \left[\|\hat{\Sigma}^{(1,1)} - \Sigma^{(1,1)}\|_F^2 \right] = \sum_{(i,j)^{(1,1)}} E \left[(\hat{\sigma}_{ij} - \sigma_{ij})^2 \right] \\
 &= \sum_{(i=j)^{(1,1)}} E \left[((1 - \lambda_1)s_{ij} + \lambda_1 s_{ij} - \sigma_{ij})^2 \right] + \sum_{(i \neq j)^{(1,1)}} E \left[((1 - \lambda_1)s_{ij} - \sigma_{ij})^2 \right] \\
 &= \sum_{(i=j)^{(1,1)}} E \left[(s_{ij} - \sigma_{ij})^2 \right] + \sum_{(i \neq j)^{(1,1)}} E \left[((1 - \lambda_1)s_{ij} - \sigma_{ij})^2 \right]
 \end{aligned}$$

Next, we use the standard identity:

$$\begin{aligned}
 \text{Var}[U] &= E[U^2] - (E[U])^2 \\
 E[U^2] &= \text{Var}[U] + (E[U])^2
 \end{aligned}$$

First, when $i \neq j$, let $U = s_{ij} - \sigma_{ij}$. Then we have

$$\begin{aligned}
 R^{(1,1)} &= \sum_{(i=j)^{(1,1)}} \text{Var}[s_{ij} - \sigma_{ij}] + (E[s_{ij} - \sigma_{ij}])^2 + \sum_{(i \neq j)^{(1,1)}} E \left[((1 - \lambda_1)s_{ij} - \sigma_{ij})^2 \right] \\
 &= \sum_{(i=j)^{(1,1)}} \text{Var}[s_{ij}] + \sum_{(i \neq j)^{(1,1)}} E \left[((1 - \lambda_1)s_{ij} - \sigma_{ij})^2 \right]
 \end{aligned}$$

where the latter line arises because s_{ij} is an unbiased estimator of σ_{ij} . Next, we consider the term when $i \neq j$, letting $U = (1 - \lambda_1)s_{ij} - \sigma_{ij}$.

$$\begin{aligned}
 R^{(1,1)} &= \sum_{(i=j)^{(1,1)}} \text{Var}[s_{ij}] + \sum_{(i \neq j)^{(1,1)}} \text{Var}[(1 - \lambda_1)s_{ij} - \sigma_{ij}] + (E[(1 - \lambda_1)s_{ij} - \sigma_{ij}])^2 \\
 &= \sum_{(i=j)^{(1,1)}} \text{Var}[s_{ij}] + \sum_{(i \neq j)^{(1,1)}} (1 - \lambda_1)^2 \text{Var}[s_{ij}] + ((1 - \lambda_1)E[s_{ij}] - \sigma_{ij})^2 \\
 &= \sum_{(i=j)^{(1,1)}} \text{Var}[s_{ij}] + \sum_{(i \neq j)^{(1,1)}} (1 - \lambda_1)^2 \text{Var}[s_{ij}] + \lambda_1^2 (E[s_{ij}])^2 \\
 &= \sum_{(i=j)^{(1,1)}} \text{Var}[s_{ij}] + \sum_{(i \neq j)^{(1,1)}} \text{Var}[s_{ij}] - 2\lambda_1 \text{Var}[s_{ij}] + \lambda_1^2 \text{Var}[s_{ij}] + \lambda_1^2 (E[s_{ij}])^2 \\
 &= \sum_{(i,j)^{(1,1)}} \text{Var}[s_{ij}] + \sum_{(i \neq j)^{(1,1)}} -2\lambda_1 \text{Var}[s_{ij}] + \lambda_1^2 E[s_{ij}^2]
 \end{aligned}$$

Case (ii): both omics variables in layer 2

In this case, we can follow the analogy to the argument above to arrive at

$$R^{(2,2)} = \sum_{(i,j)^{(2,2)}} \text{Var}[s_{ij}] + \sum_{(i \neq j)^{(2,2)}} -2\lambda_2 \text{Var}[s_{ij}] + \lambda_2^2 E[s_{ij}^2] \quad (3)$$

Case (iii): variable i is in omics layer 1 and variable j is in omics layer 2.

In this case, we derive $R^{(1,2)}$, noting that $R^{(2,1)} = R^{(1,2)}$ by symmetry.

$$\begin{aligned} R^{(1,2)} &= E \left[\|\hat{\Sigma}^{(1,2)} - \Sigma^{(1,2)}\|_F^2 \right] \\ &= \sum_{(i,j)^{(1,2)}} E [(\hat{\sigma}_{ij} - \sigma_{ij})^2] \\ &= \sum_{(i,j)^{(1,2)}} \text{Var}[\hat{\sigma}_{ij} - \sigma_{ij}] + (E[\hat{\sigma}_{ij} - \sigma_{ij}])^2 \\ &= \sum_{(i,j)^{(1,2)}} (1 - \lambda_1)(1 - \lambda_2) \text{Var}[s_{ij}] + (E[\hat{\sigma}_{ij} - s_{ij} + s_{ij} - \sigma_{ij}])^2 \\ &= \sum_{(i,j)^{(1,2)}} (1 - \lambda_1)(1 - \lambda_2) \text{Var}[s_{ij}] + (E[\sqrt{1 - \lambda_1} \sqrt{1 - \lambda_2} s_{ij} - s_{ij}] + E[s_{ij} - \sigma_{ij}])^2 \\ &= \sum_{(i,j)^{(1,2)}} (1 - \lambda_1)(1 - \lambda_2) \text{Var}[s_{ij}] + (\sqrt{1 - \lambda_1} \sqrt{1 - \lambda_2} - 1)^2 (E[s_{ij}])^2 \end{aligned}$$

Now the expression is in terms of the variance and expectation of the sample covariance, which we can easily approximate with moment estimators. We continue manipulating the expression:

$$\begin{aligned} R^{(1,2)} &= \sum_{(i,j)^{(1,2)}} \{1 - \lambda_1 - \lambda_2 + \lambda_1 \lambda_2\} \text{Var}[s_{ij}] + \left\{ (1 - \lambda_1)(1 - \lambda_2) - 2\sqrt{1 - \lambda_1} \sqrt{1 - \lambda_2} + 1 \right\} (E[s_{ij}])^2 \\ &= \sum_{(i,j)^{(1,2)}} \{1 - \lambda_1 - \lambda_2 + \lambda_1 \lambda_2\} \text{Var}[s_{ij}] + \left\{ 2 - \lambda_1 - \lambda_2 + \lambda_1 \lambda_2 - 2\sqrt{1 - \lambda_1} \sqrt{1 - \lambda_2} \right\} (E[s_{ij}])^2 \end{aligned}$$

Next, we again apply the identity $(E[U])^2 = E[U^2] - \text{Var}[U]$:

$$\begin{aligned}
&= \sum_{(i,j)^{(1,2)}} \{1 - \lambda_1 - \lambda_2 + \lambda_1 \lambda_2\} \text{Var}[s_{ij}] + \left\{2 - \lambda_1 - \lambda_2 + \lambda_1 \lambda_2 - 2\sqrt{1 - \lambda_1} \sqrt{1 - \lambda_2}\right\} (E[s_{ij}^2] - \text{Var}[s_{ij}]) \\
&= \sum_{(i,j)^{(1,2)}} \left\{1 - \lambda_1 - \lambda_2 + \lambda_1 \lambda_2 - (2 - \lambda_1 - \lambda_2 + \lambda_1 \lambda_2 - 2\sqrt{1 - \lambda_1} \sqrt{1 - \lambda_2})\right\} \text{Var}[s_{ij}] \\
&+ \left\{2 - \lambda_1 - \lambda_2 + \lambda_1 \lambda_2 - 2\sqrt{1 - \lambda_1} \sqrt{1 - \lambda_2}\right\} E[s_{ij}^2] \\
&= \sum_{(i,j)^{(1,2)}} \left\{-1 + 2\sqrt{1 - \lambda_1} \sqrt{1 - \lambda_2}\right\} \text{Var}[s_{ij}] + \left\{2 - \lambda_1 - \lambda_2 + \lambda_1 \lambda_2 - 2\sqrt{1 - \lambda_1} \sqrt{1 - \lambda_2}\right\} E[s_{ij}^2] \\
&= - \sum_{(i,j)^{(1,2)}} \text{Var}[s_{ij}] + 2\sqrt{1 - \lambda_1} \sqrt{1 - \lambda_2} \sum_{(i,j)^{(1,2)}} (\text{Var}[s_{ij}] - E[s_{ij}^2]) + (2 - \lambda_1 - \lambda_2 + \lambda_1 \lambda_2) \sum_{(i,j)^{(1,2)}} E[s_{ij}^2]
\end{aligned}$$

Combining cases (i), (ii), and (iii)

Our final expression for R is

$$\begin{aligned}
R &= R^{(1,1)} + R^{(2,2)} + 2R^{(1,2)} \\
&= \sum_{(i,j)^{(1,1)}} \text{Var}[s_{ij}] + \sum_{(i \neq j)^{(1,1)}} -2\lambda_1 \text{Var}[s_{ij}] + \lambda_1^2 E[s_{ij}^2] \\
&+ \sum_{(i,j)^{(2,2)}} \text{Var}[s_{ij}] + \sum_{(i \neq j)^{(2,2)}} -2\lambda_2 \text{Var}[s_{ij}] + \lambda_2^2 E[s_{ij}^2] \\
&+ 2 * \left\{ - \sum_{(i,j)^{(1,2)}} \text{Var}[s_{ij}] + 2\sqrt{1 - \lambda_1} \sqrt{1 - \lambda_2} \sum_{(i,j)^{(1,2)}} (\text{Var}[s_{ij}] - E[s_{ij}^2]) + (2 - \lambda_1 - \lambda_2 + \lambda_1 \lambda_2) \sum_{(i,j)^{(1,2)}} E[s_{ij}^2] \right\} \\
&= \sum_{(i \neq j)^{(1,1)}} -2\lambda_1 \text{Var}[s_{ij}] + \lambda_1^2 E[s_{ij}^2] + \sum_{(i,j)^{(2,2)}} \text{Var}[s_{ij}] - 2\lambda_2 \text{Var}[s_{ij}] + \lambda_2^2 E[s_{ij}^2] \\
&+ 4\sqrt{1 - \lambda_1} \sqrt{1 - \lambda_2} \sum_{(i,j)^{(1,2)}} (\text{Var}[s_{ij}] - E[s_{ij}^2]) \\
&+ 2 * (2 - \lambda_1 - \lambda_2 + \lambda_1 \lambda_2) \sum_{(i,j)^{(1,2)}} E[s_{ij}^2]
\end{aligned}$$

Combining like terms for functions of λ_1 and λ_2 , we can write

$$\begin{aligned}
 R &= \sum_{(i \neq j)^{(1,1)}} -2\lambda_1 \text{Var}[s_{ij}] + \lambda_1^2 E[s_{ij}^2] + \sum_{(i \neq j)^{(2,2)}} -2\lambda_2 \text{Var}[s_{ij}] + \lambda_2^2 E[s_{ij}^2] \\
 &+ 4\sqrt{1-\lambda_1}\sqrt{1-\lambda_2} \sum_{(i,j)^{(1,2)}} (\text{Var}[s_{ij}] - E[s_{ij}^2]) \\
 &+ 2 * (2 - \lambda_1 - \lambda_2 + \lambda_1 \lambda_2) \sum_{(i,j)^{(1,2)}} E[s_{ij}^2] \\
 &= 4 \sum_{(i,j)^{(1,2)}} E[s_{ij}^2] \\
 &+ \lambda_1 \left\{ -2 \sum_{(i \neq j)^{(1,1)}} \text{Var}[s_{ij}] - 2 \sum_{(i,j)^{(1,2)}} E[s_{ij}^2] \right\} \\
 &+ \lambda_2 \left\{ -2 \sum_{(i \neq j)^{(2,2)}} \text{Var}[s_{ij}] - 2 \sum_{(i,j)^{(1,2)}} E[s_{ij}^2] \right\} \\
 &+ \lambda_1^2 \sum_{(i \neq j)^{(1,1)}} E[s_{ij}^2] \\
 &+ \lambda_2^2 \sum_{(i \neq j)^{(2,2)}} E[s_{ij}^2] \\
 &+ \lambda_1 \lambda_2 \left\{ 2 \sum_{(i,j)^{(1,2)}} E[s_{ij}^2] \right\} \\
 &+ \sqrt{1-\lambda_1}\sqrt{1-\lambda_2} \left\{ 4 \sum_{(i,j)^{(1,2)}} (\text{Var}[s_{ij}] - E[s_{ij}^2]) \right\}
 \end{aligned}$$

This expression is of the form

$$R = \text{const.} + \lambda_1 T_1^{(1)} + \lambda_2 T_1^{(2)} + \lambda_1^2 T_2^{(1)} + \lambda_1^2 T_2^{(2)} + \lambda_1 \lambda_2 T_3 + \sqrt{1-\lambda_1}\sqrt{1-\lambda_2} T_4 \quad (4)$$

where the first term is a constant with respect to λ_1 and λ_2 and the remaining terms T are defined as:

$$\begin{aligned}
 T_1^{(k)} &= -2 \left(\sum_{(i \neq j)^{(k,k)}} \text{Var}[s_{ij}] + \sum_{(i,j)^{(1,2)}} E[s_{ij}^2] \right); k = 1, 2 \\
 T_2^{(k)} &= \sum_{(i \neq j)^{(k,k)}} E[s_{ij}^2]; k = 1, 2 \\
 T_3 &= 2 \sum_{(i,j)^{(1,2)}} E[s_{ij}^2] \\
 T_4 &= 4 \sum_{(i,j)^{(1,2)}} (\text{Var}[s_{ij}] - E[s_{ij}^2])
 \end{aligned}$$

2. Simulation study to illustrate partial correlations

We first simulated normal distributed values of the “regulator” via $regulator \sim N(\mu = 0, \sigma = 1)$. Then we defined gene A and B to equal $regulator + \epsilon_{A,B}$, respectively, where $\epsilon_{A,B} \sim N(\mu = 0, \sigma = .1)$. Simulations were performed using the R programming environment version 4.1.2 [1]. For ordinary partial correlation estimates, we used the R package “ppcor” [2].

3. Supplementary figures for simulation studies

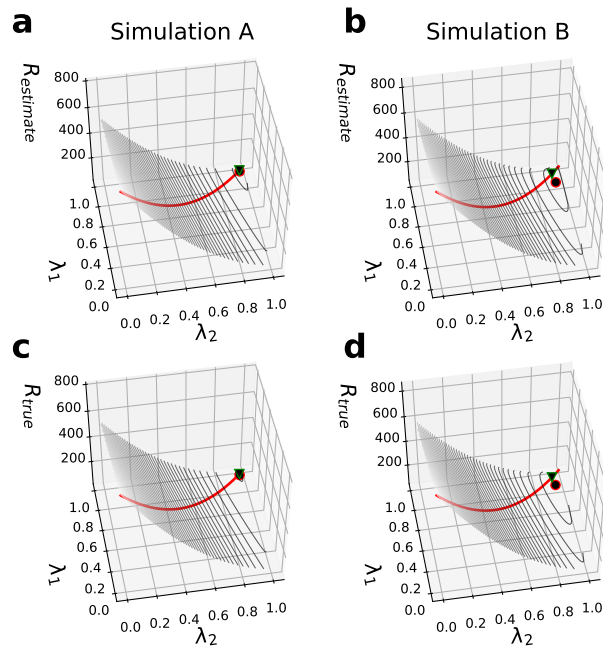


Figure S1: Parameter landscapes for DRAGON in studies A and B . The plot is understood analogous to Figure 2 in the main article but now for $n = 500$.

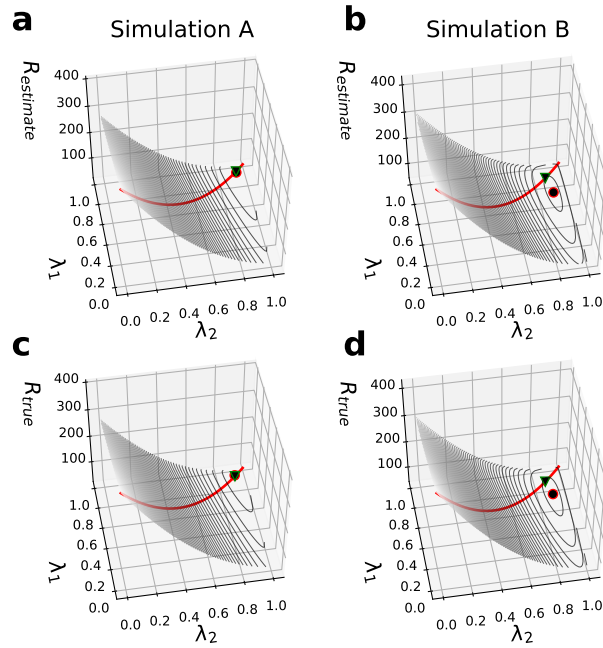


Figure S2: Parameter landscapes for DRAGON in studies *A* and *B*. The plot is understood analogous to Figure 2 in the main article but now for $n = 1,000$.

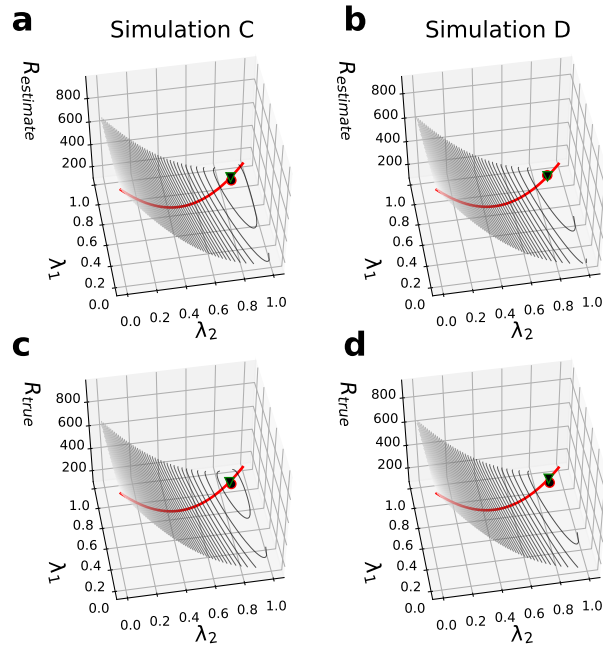


Figure S3: Parameter landscapes for DRAGON. Estimated and true R (upper and lower row) in dependency of λ_1 and λ_2 in simulation studies *C* (left column) and *D* (right column) for $n = 500$. Figures a and b show the estimated R for studies *C* and *D*, respectively. Figures c and d show the corresponding ground truth. The red circles indicate the minima for each plot in the λ_1 – λ_2 plane, and the green triangles give the minima on the diagonal R values shown in red, corresponding to the standard GGM.

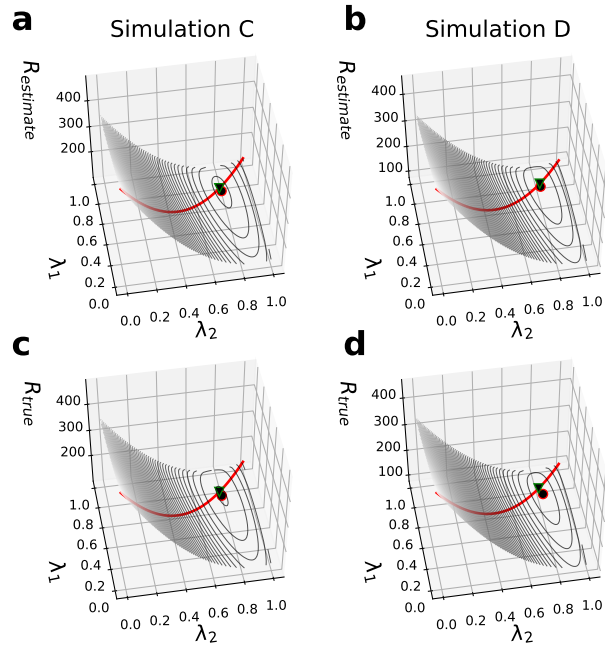


Figure S4: Parameter landscapes for DRAGON in studies *C* and *D*. The plot is understood analogous to Figure S5 but now for $n = 1,000$.

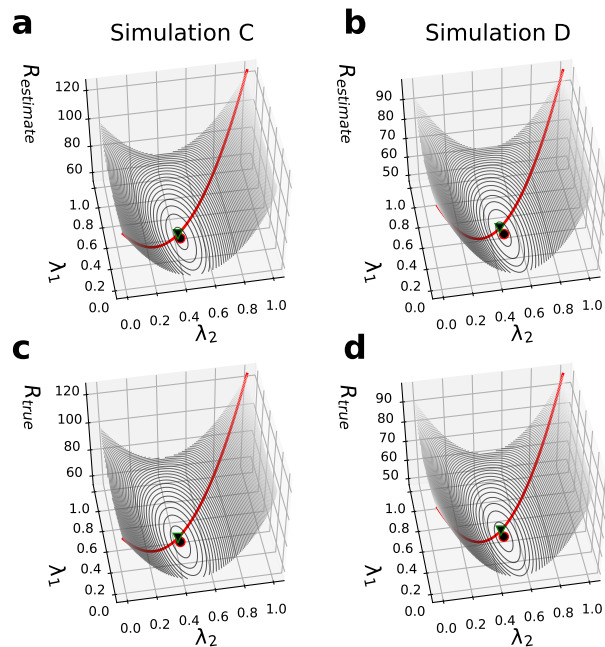


Figure S5: Parameter landscapes for DRAGON in studies *C* and *D*. The plot is understood analogous to Figure S5 but now for $n = 5,000$.

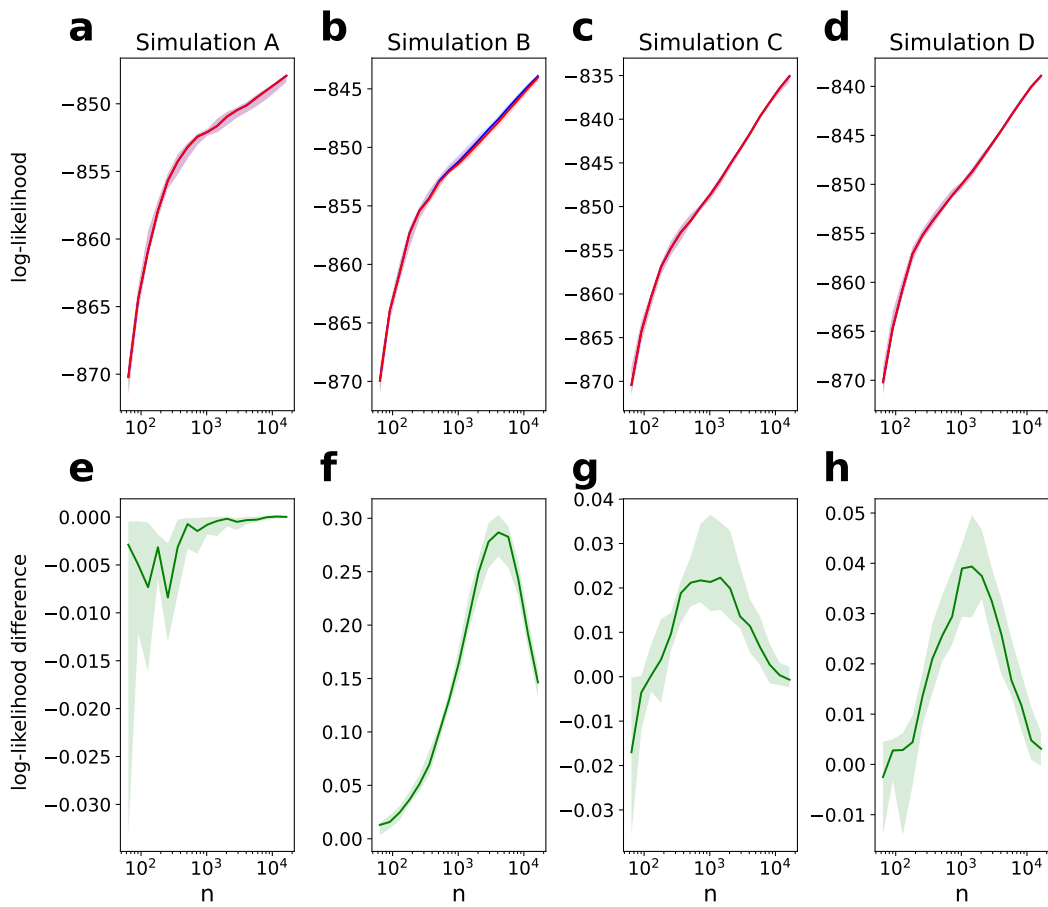


Figure S6: Log-likelihood comparison between DRAGON and GGM. The upper row, Figures a to d give the log-likelihood evaluated on test data versus the number of training samples, n , for simulation studies A to D, respectively. Results from DRAGON are given in blue and those from the GGM in red. The lines correspond to the median log-likelihood and the bands to the 25% and 75% percentiles of the distribution. Figures e to h show the corresponding log-likelihood differences (DRAGON minus GGM) in green.

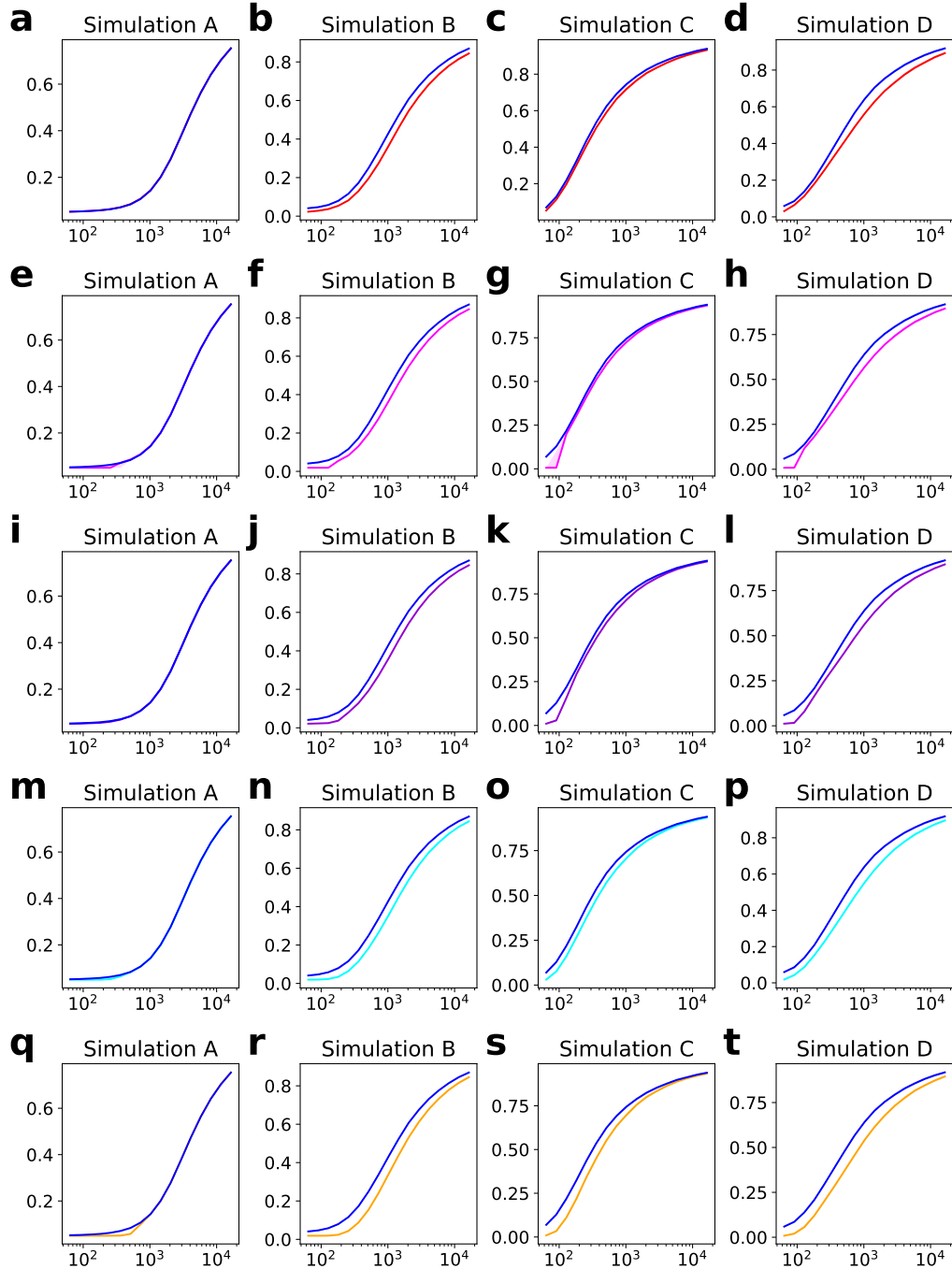


Figure S7: Area under the precision-recall curve (AUC-PR) for edge-recovery performance versus sample size n of simulation studies A to D (columns). Each row compares DRAGON (blue) with GGM (red, Fig. a to d), GeneNet (magenta, Fig. e to h), B-NW-SL (purple, Fig. i to l), D-S-NW-SL (cyan, Fig. m to p), and D-S-GL (orange, Fig. q to t), respectively. The lines correspond to the median AUC-PR and the bands to the 25% and 75% percentiles of the distribution.

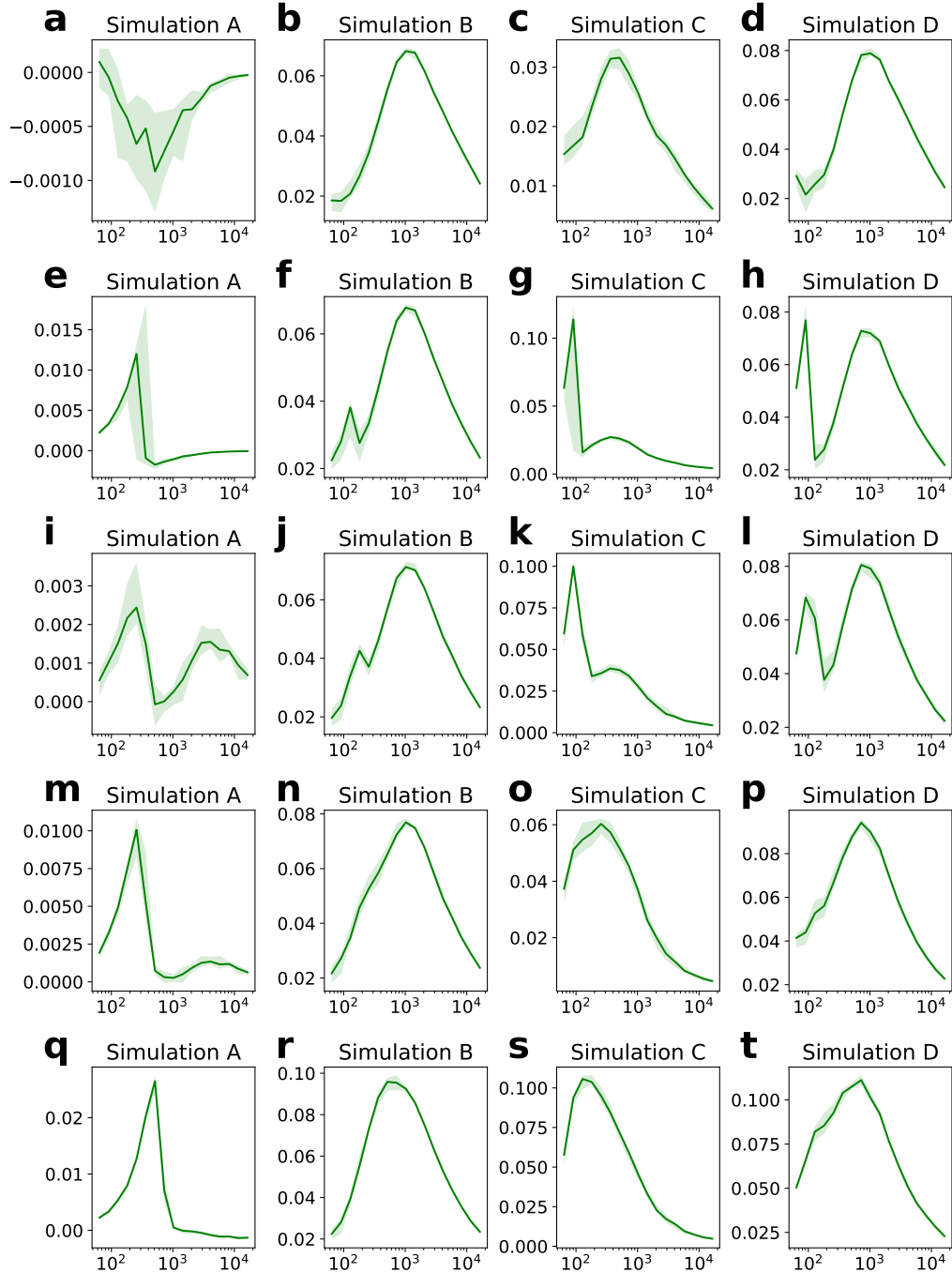


Figure S8: Area under the precision-recall curve (AUC-PR) differences versus sample size n of simulation studies *A* to *D* (columns). Each row corresponds to the AUC-PR difference DRAGON minus GGM (Fig. a to d), DRAGON minus GeneNet (Fig. e to h), DRAGON minus B-NW-SL (Fig. i to l), DRAGON minus D-S-NW-SL (Fig. m to p), and DRAGON minus D-S-GL (Fig. q to t), respectively. The green lines correspond to the median AUC-PR and the bands to the 25% and 75% percentiles of the distribution.

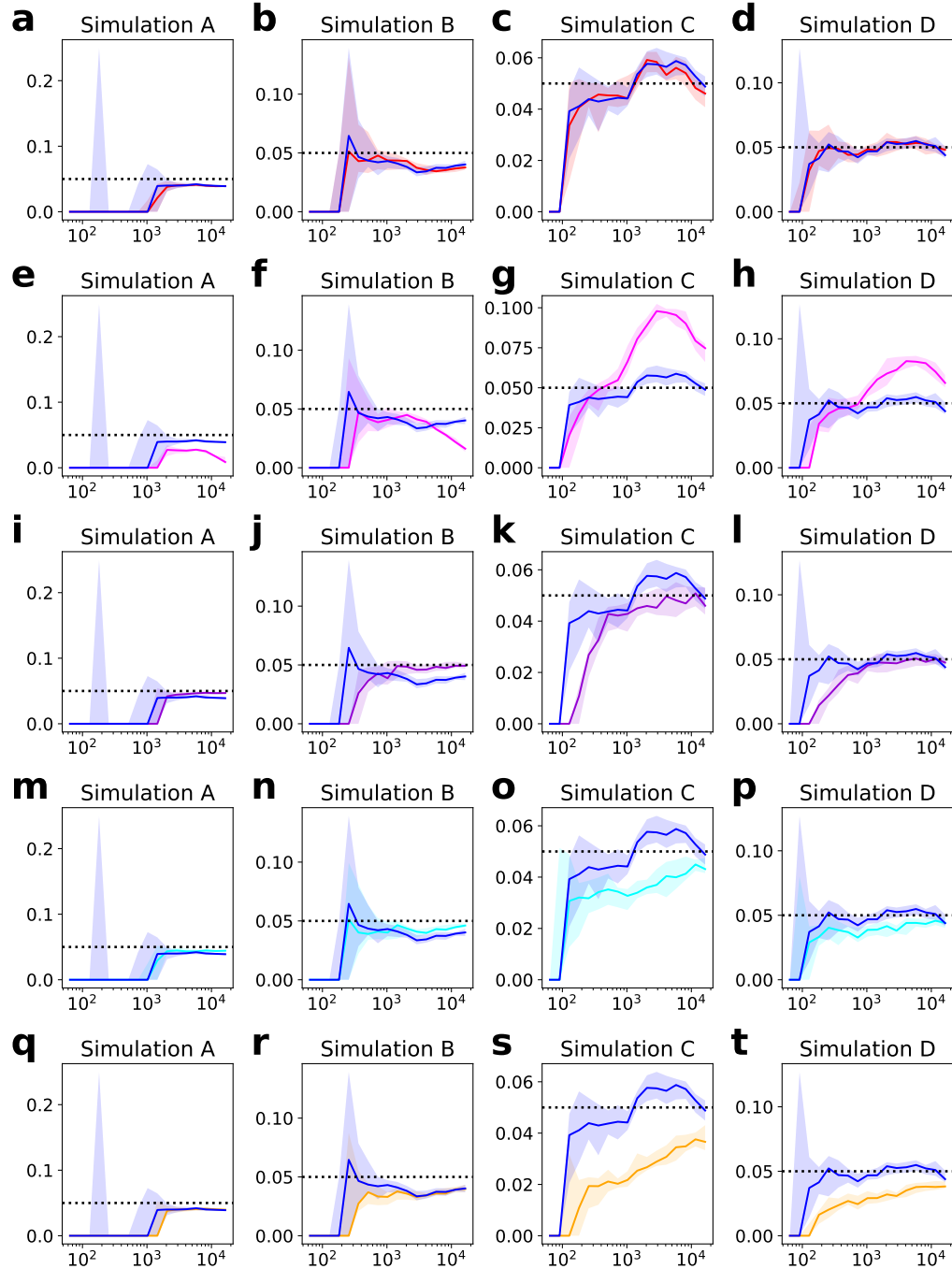


Figure S9: Posterior False-discovery rates (FDRs) versus sample size n of simulation studies *A* to *D* (columns) for significance threshold $\alpha = 0.05$ (dotted line). Each row compares DRAGON (blue) with GGM (red, Fig. a to d), GeneNet (magenta, Fig. e to h), B-NW-SL (purple, Fig. i to l), D-S-NW-SL (cyan, Fig. m to p), and D-S-GL (orange, Fig. q to t), respectively. The lines correspond to the median FDR and the bands to the 25% and 75% percentiles of the distribution.

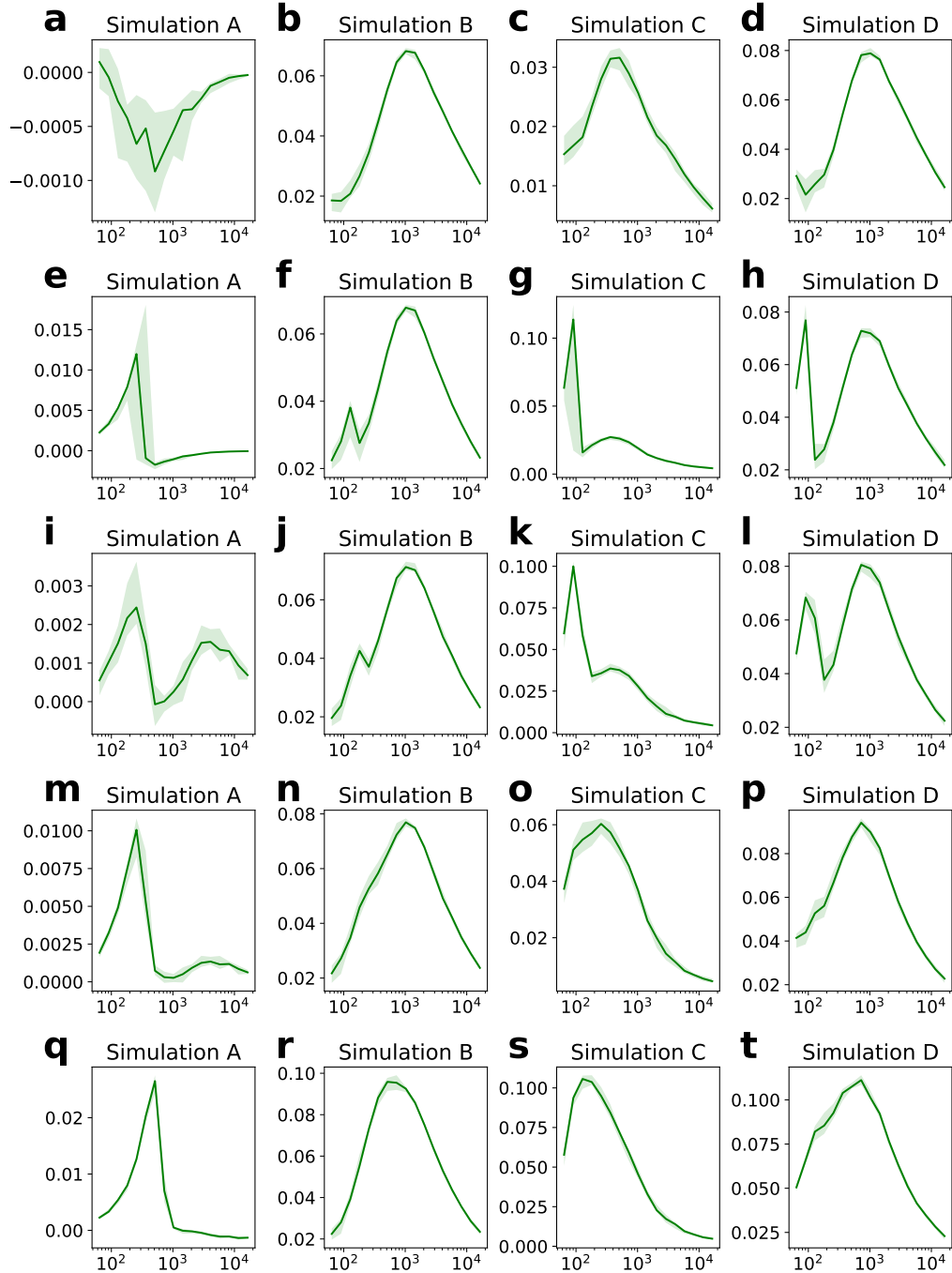


Figure S10: False-discovery rates (FDRs) differences versus sample size n of simulation studies A to D (columns). Each row corresponds to the FDR difference DRAGON minus GGM (Fig. a to d), DRAGON minus GeneNet (Fig. e to h), DRAGON minus B-NW-SL (Fig. i to l), DRAGON minus D-S-NW-SL (Fig. m to p), and DRAGON minus D-S-GL (Fig. q to t), respectively. The green lines correspond to the median FDR and the bands to the 25% and 75% percentiles of the distribution.

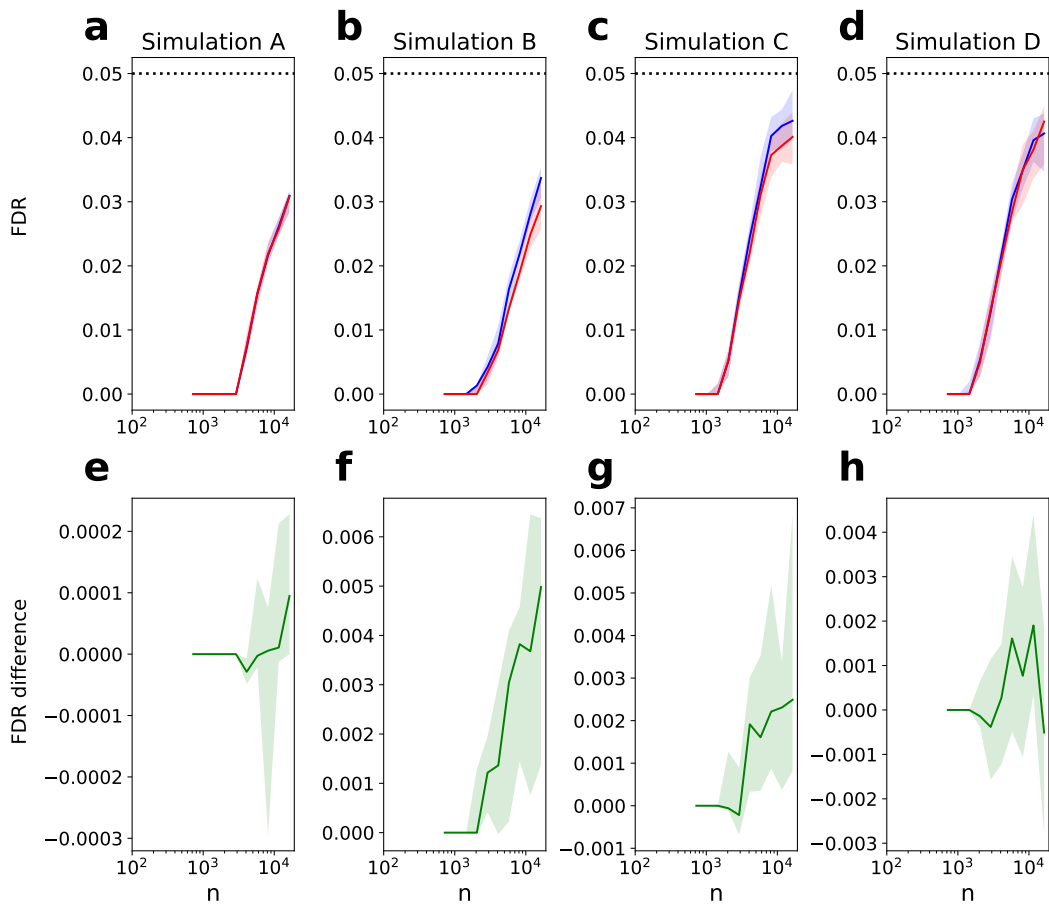


Figure S11: As Figure S9a to d and S10a to d but now using the theoretical value $\kappa = n - 1 - (p - 2)$ to estimate significance levels.

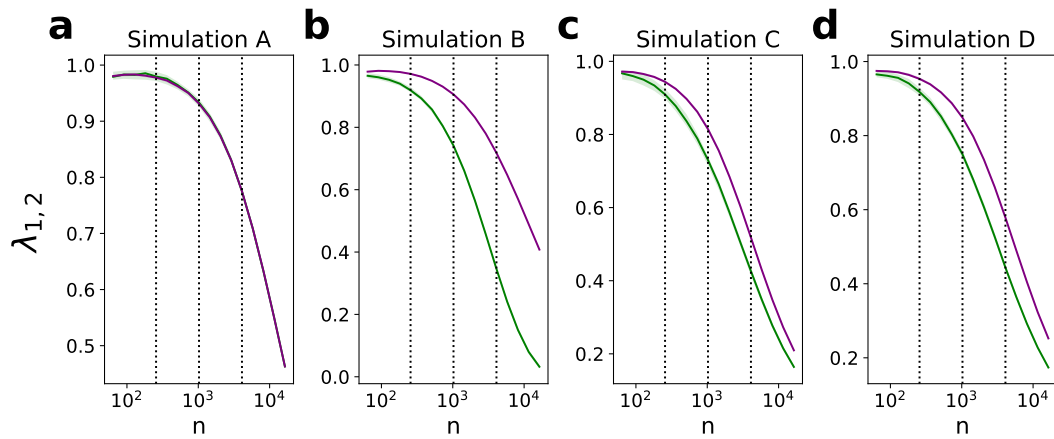


Figure S12: Regularization parameters λ_1 (green) and λ_2 (purple) for simulation studies A to D for different sample sizes. The vertical, dotted lines correspond to $n = 256$, $n = 1,024$, and $n = 4,096$. The respective pairs (λ_1, λ_2) were evaluated to verify that p -value distributions are flat under the null hypothesis ($H_0 : \rho = 0$).

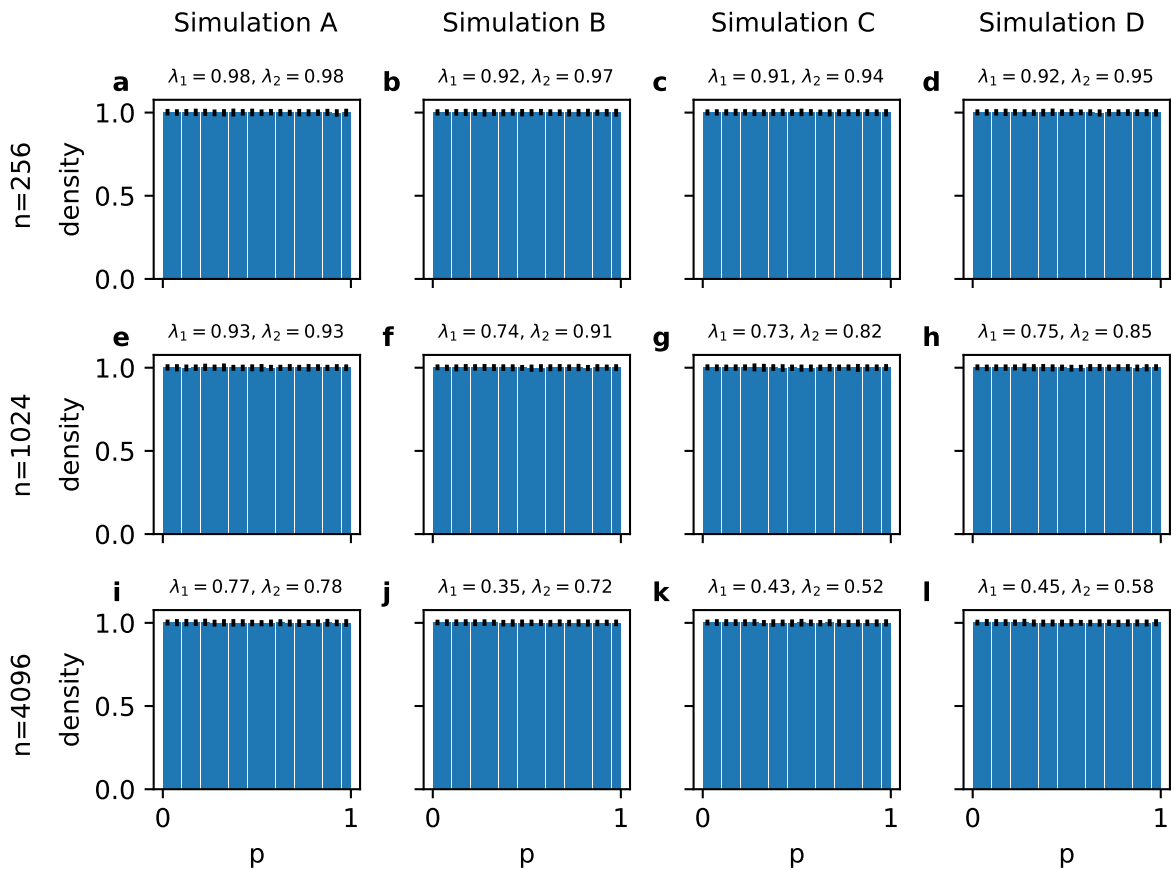


Figure S13: Distributions of p -values estimated by DRAGON for data simulated under the null hypothesis ($H_0 : \rho = 0$) for given pairs of the regularization parameters λ_1 and λ_2 . The (λ_1, λ_2) -pairs are given at the top of Figures a to l and were derived as described in the main article, cf. also Figure S12. Their corresponding sample size n and simulation study are given at the left side and at the top, respectively. Error bars represent ± 1 standard deviation across 10 simulation runs.

4. TCGA analysis dataset

The dataset consists of one primary tumor sample from each of 765 women. The distribution of subtype, race, and ethnicity are shown below in Table S1.

mRNA subtype		
	Basal	132
	Her2	46
	Luminal A	412
	Luminal B	141
	Normal	34
Race		
	American Indian or Alaska Native	1
	Asian	38
	Black or African American	157
	White	554
	Not reported	15
Ethnicity		
	Hispanic or Latino	36
	Not Hispanic or Latino	661
	Not reported	68

Table S1: Basic characteristics of the TCGA dataset used in the breast cancer example.

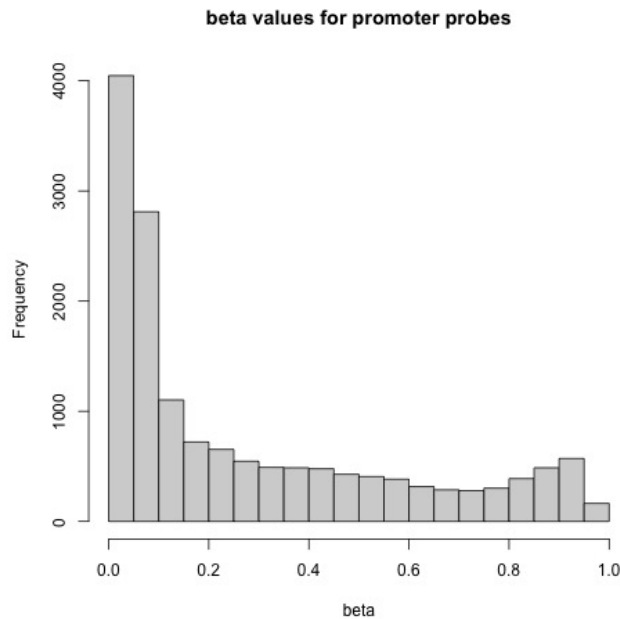


Figure S14: Distribution of mean promoter across TFs in our analysis.

5. Preprocessing of TCGA methylation data

Mapping array probes to TF promoters

The TCGA methylation files consist of one beta value per probe per sample. In this application, we consider promoter methylation of transcription factors (TFs) only. To construct one methylation value per TF per sample, we first filtered probes to only those probes within 1500 base pairs upstream of the transcription start site (TSS) for each TF. Next, probes meeting this criterion for more than one TF were mapped to the closest downstream TF. Finally, the beta values for each probe in the promoter region for each TF were averaged within each sample, yielding one methylation value per TF per sample.

Distribution of promoter methylation values

The distribution of these methylation values for each of the 1590 TFs in our dataset is shown in Supplementary Figure S14. Rather than the typical bimodal distribution expected in methylation data, these methylation values tend towards a right-skewed, unimodal distribution. This may be due to the fact that all samples are from cancerous tissue and promoter hypomethylation (particularly in CpG islands) is characteristic of cancers [3]. This hypothesis is supported by the distribution of the individual probes across CpG island labels (island, shelves, and shores; Supplementary Figure S15).

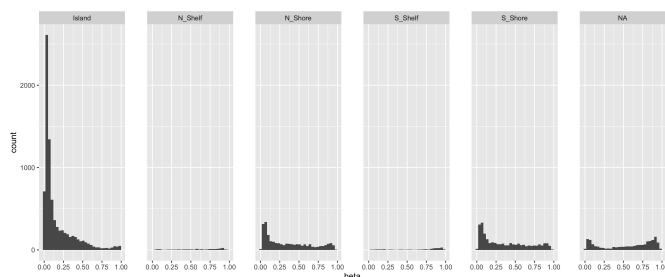


Figure S15: The distribution of methylation beta values shows an emphasis on probes in CpG islands and a general trend of hypomethylation in probes annotated to islands, shelves, and shores vs. probes without a CpG island-related annotation ('NA').

Missing data and data transformation

Genes missing beta values for greater than 20 percent of the samples were removed from the analysis (N=33). For genes missing from $\leq 20\%$ of the samples, missing promoter beta values were imputed with mean imputation. Prior to input into DRAGON, promoter methylation was transformed to approximate Gaussianity using the nonparanormal transformation in the R package huge [4, 5].

6. Preprocessing of TCGA RNA-seq data

No measures of TPM were missing in the gene expression data; however, many counts had a value of 0 or 1 TPM. We included only TFs that were expressed with $\text{TPM} > 1$ in at least 20 percent of the data. This criterion omitted 318 of the TFs. TPMs were transformed to an approximately Gaussian distribution using a log transformation. To handle the cases where $\text{TPM}=0$, we set the transformed TPM equal to $\log(\text{TPM}+1)$.

7. Summary of DRAGON model

We ran DRAGON on 765 samples of 1311 gene expression measurements and 1557 gene-level methylation measurements after preprocessing as described above. Recall that DRAGON does not require measurements on the same variables across omics layers; here, both expression and methylation levels were available for 1297 genes.

The optimal tuning parameters were determined to be $\lambda_1 = 0.058$ and $\lambda_2 = 0.031$, where λ_1 governs the shrinkage of the methylation data and λ_2 governs the shrinkage of the gene expression data. The estimated parameters of the probability distribution in Equation (10) of the main manuscript were $\kappa_{11} = 12725.61$, $\kappa_{22} = 5175.30$, and $\kappa_{12} = 815.94$.

8. Community detection methodology

Community detection was performed using the `cluster_fast_greedy` algorithm as implemented in the `igraph` R package [6, 7]. In this algorithm, the weight of an edge in the graph represents the strength of

the connection between two nodes. Because the DRAGON network contains both positive and negative edge weights, edge weights were transformed to their absolute value prior to community detection. This transformation reflects the paradigm that we are interested in communities of nodes that are conditionally associated, not whether the association is positive or negative.

To conduct the over-representation analysis, the `fora` function of the `fgsea` R package was used[8]. Reactome gene sets with at least 3 genes were considered (`minSize = 3`). Importantly, a single TF may be represented by two separate nodes in the DRAGON network, one representing its methylation and one representing its expression. Therefore, the universe of possible genes considered for the ORA has twice the size of the number of TFs included in the DRAGON model and consists of two entries for each TF: one corresponding to its methylation and one corresponding to its expression. We additionally considered an ORA assessing enrichment for methylation only and one assessing enrichment for expression only. A Reactome pathway was considered to be over-represented in a community if its FDR was less than 0.05 in at least one of these three methods (Benjamini-Hochberg FDR as implemented in `fgsea`).

9. BRCA hub nodes

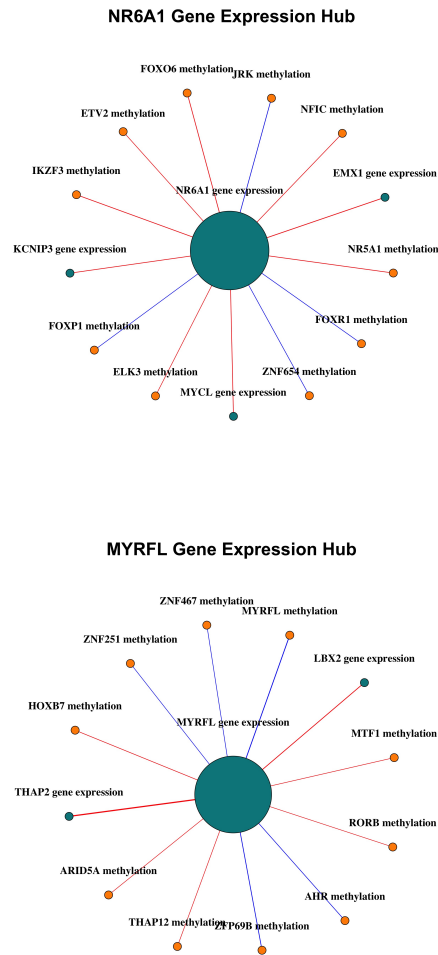


Figure S16: Neighborhoods of NR6A1 and MYRFL in the DRAGON breast cancer network. Turquoise nodes represent gene expression and orange nodes represent promoter methylation. Larger nodes have higher node degrees. Edges with $FDR < 0.05$ are shown.

10. Community analysis

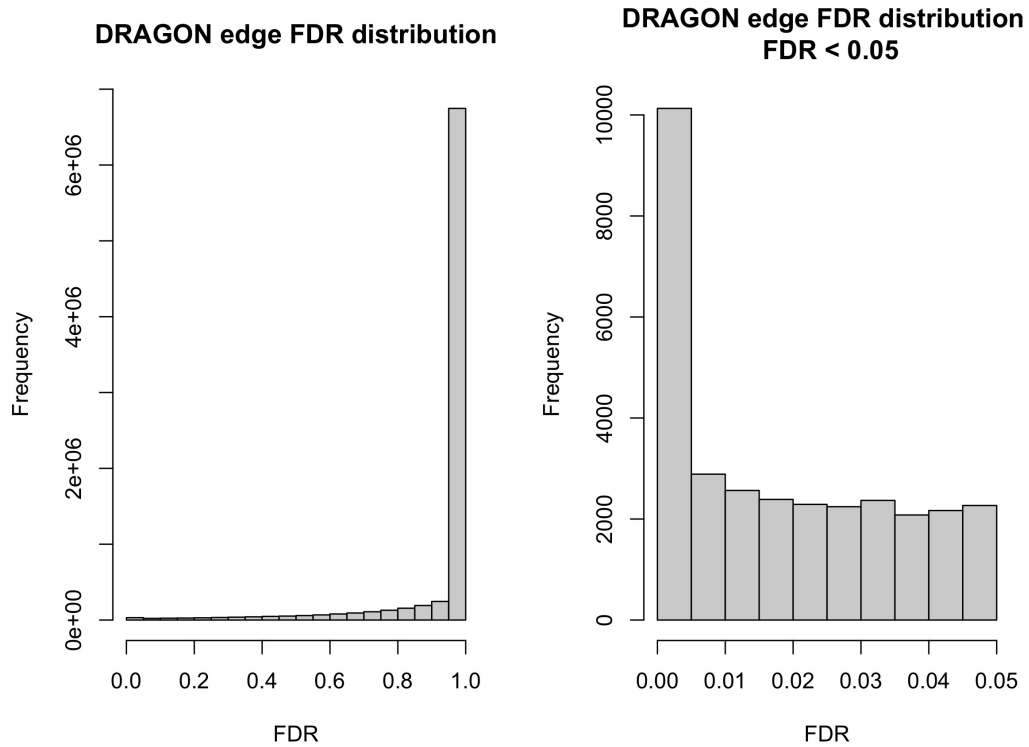


Figure S17: Distribution of Benjamini-Hochberg adjusted p -values (FDR) for the DRAGON BRCA network. Based on the shape of this distribution, edges with $FDR < 0.005$ were considered true edges and carried forward in the analysis.

DRAGON Supplementary Material

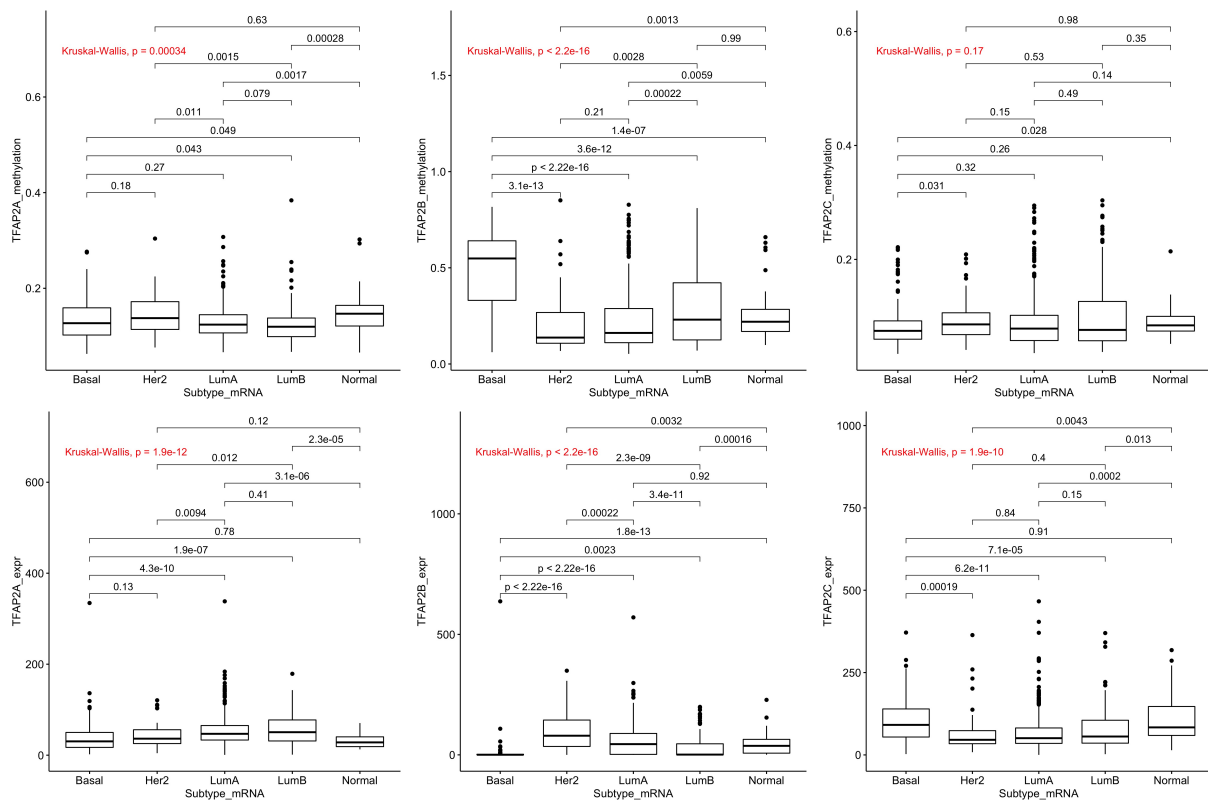


Figure S18: Subtype-specific methylation and expression of TFAP2 family transcription factors, which are key players in the enrichment analysis for Community 5.

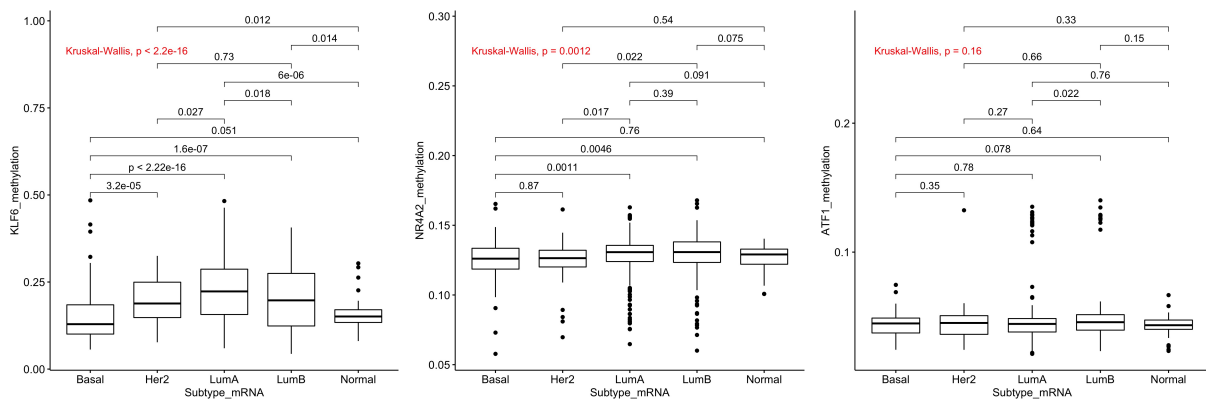


Figure S19: Subtype-specific methylation of key methylation nodes in Community 38 (KLF6 and NR4A2), vs. subtype-specific methylation of a housekeeping gene (ATF1).

References

- [1] R Core Team. *R: A Language and Environment for Statistical Computing*. R Foundation for Statistical Computing, Vienna, Austria, 2021.
- [2] Seongho Kim. *ppcor: Partial and Semi-Partial (Part) Correlation*, 2015. R package version 1.1.
- [3] Emmanouil Bouras, Meropi Karakioulaki, Konstantinos I Bougioukas, Michalis Aivaliotis, Georgios Tzimagiorgis, and Michael Chourdakis. Gene promoter methylation and cancer: An umbrella review. *Gene*, 710:333–340, 2019.
- [4] Han Liu, John Lafferty, and Larry Wasserman. The nonparanormal: Semiparametric estimation of high dimensional undirected graphs. *Journal of Machine Learning Research*, 10(Oct):2295–2328, 2009.
- [5] Tuo Zhao, Han Liu, Kathryn Roeder, John Lafferty, and Larry Wasserman. The huge package for high-dimensional undirected graph estimation in r. *The Journal of Machine Learning Research*, 13:1059–1062, 2012.
- [6] Pascal Pons and Matthieu Latapy. Computing communities in large networks using random walks. In *International symposium on computer and information sciences*, pages 284–293. Springer, 2005.
- [7] Gabor Csardi, Tamas Nepusz, et al. The igraph software package for complex network research. *InterJournal, complex systems*, 1695(5):1–9, 2006.
- [8] Gennady Korotkevich, Vladimir Sukhov, Nikolay Budin, Boris Shpak, Maxim N Artyomov, and Alexey Sergushichev. Fast gene set enrichment analysis. *BioRxiv*, page 060012, 2021.